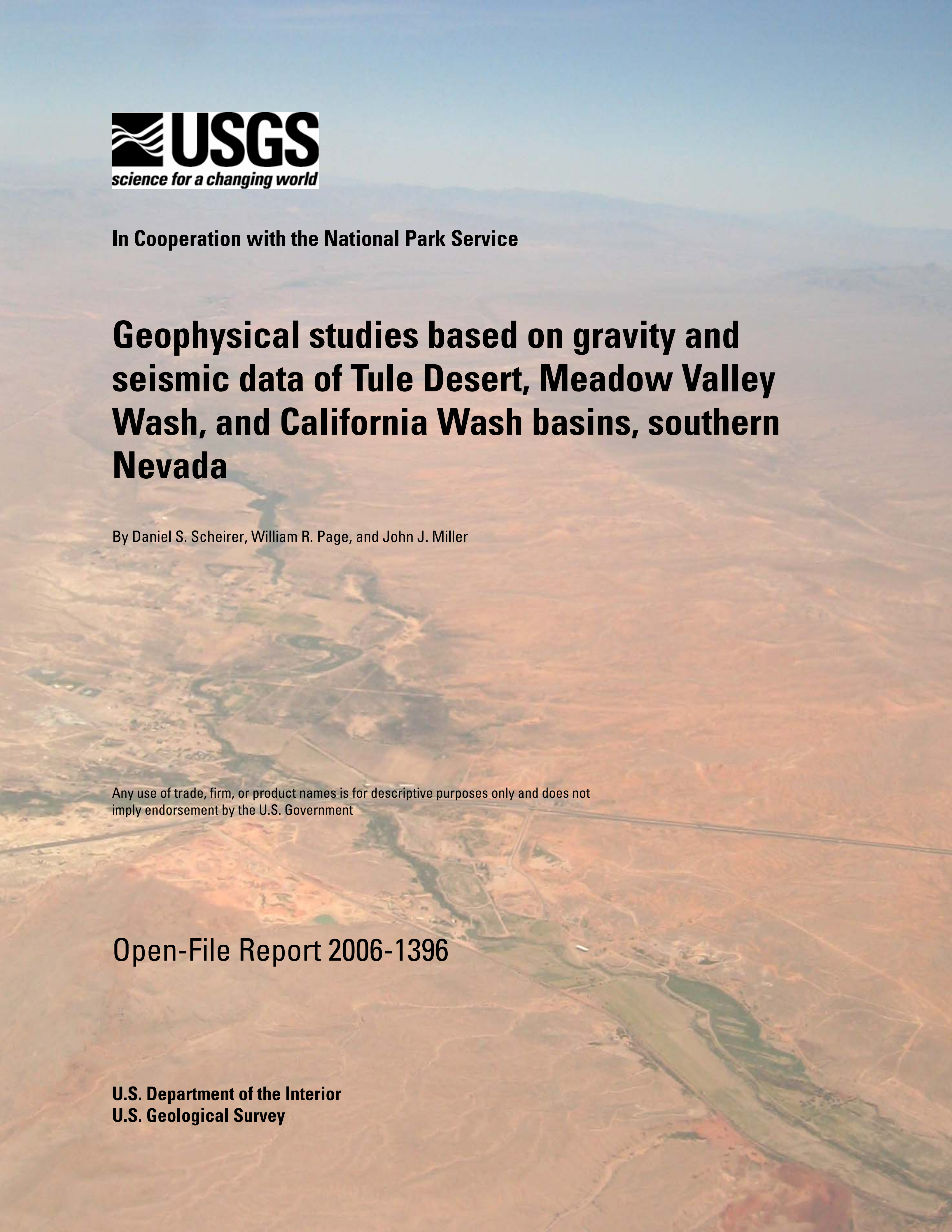

In Cooperation with the National Park Service

Geophysical studies based on gravity and seismic data of Tule Desert, Meadow Valley Wash, and California Wash basins, southern Nevada

By Daniel S. Scheirer, William R. Page, and John J. Miller

Open-File Report 2006-1396

U.S. Department of the Interior
U.S. Geological Survey

Contents

Figures

Tables

Geophysical studies based on gravity and seismic data of Tule Desert, Meadow Valley Wash, and California Wash basins, southern Nevada

By Daniel S. Scheirer, William R. Page, and John J. Miller

Abstract

Gravity and seismic data from Tule Desert, Meadow Valley Wash, and California Wash, Nevada, provide insight into the subsurface geometry of these three basins that lie adjacent to rapidly-developing areas of Clark County, Nevada. Each of the basins is the product of Tertiary extension accommodated with the general form of north-south oriented, asymmetrically-faulted half-grabens. Geophysical inversion of gravity observations indicates that Tule Desert and Meadow Valley Wash basins are segmented into subbasins by shallow, buried basement highs. In this study, “basement” refers to pre-Cenozoic bedrock units that underlie basins filled with Cenozoic sedimentary and volcanic units. In Tule Desert, a small, buried basement high inferred from gravity data appears to be a horst whose placement is consistent with seismic reflection and magnetotelluric observations. Meadow Valley Wash consists of three subbasins separated by basement highs at structural zones that accommodated different styles of extension of the adjacent subbasins, an interpretation consistent with geologic mapping of fault traces oblique to the predominant north-south fault orientation of Tertiary extension in this area. California Wash is a single structural basin. The three seismic reflection lines analyzed in this study image the sedimentary basin fill, and they allow identification of faults that offset basin deposits and underlying basement. The degree of faulting and folding of the basin-fill deposits increases with depth. Pre-Cenozoic units are observed in some of the seismic reflection lines, but their reflections are generally of poor quality or are absent. Factors that degrade seismic reflector quality in this area are rough land topography due to erosion, deformed sedimentary units at the land surface, rock layers that dip out of the plane of the seismic profile, and the presence of volcanic units that obscure underlying reflectors. Geophysical methods illustrate that basin geometry is more complicated than would be inferred from extrapolation of surface topography and geology, and these methods aid in defining a three-dimensional framework to understand groundwater storage and flow in southern Nevada.

Introduction and Geologic Setting

The geologic configuration of southern Nevada is complex, the result of multiple episodes of marine and non-marine sedimentation, igneous activity, and contractional, strike-slip, and extensional deformation from Precambrian time to the present. In recent decades, rapid urbanization in Clark County, Nev., has led to increased demand for surface water and groundwater resources in southern Nevada. Numerous studies have endeavored to understand the hydrogeologic framework that influences groundwater distribution and flow. The present study is a geophysical companion to a recent geologic map synthesis (Page and others, 2005) and a report of interpretive geologic cross-sections (Page and others, 2006) that focus on the lithologic and structural features that allow or impede groundwater flow in southern Nevada.

The Great Basin has been subdivided into a number of large groundwater flow systems (e.g. Harrill and others, 1988), each encompassing many valleys and ranges. Recharge of these systems occurs from precipitation, primarily in mountainous areas. A key concept of these flow systems is that groundwater can flow between topographic basins (e.g. Eakin and Winograd, 1965). Discharge from the flow systems commonly occurs in springs or at rivers that may be distally located from recharge areas. The primary aquifer of the southern Great Basin is hosted by Paleozoic carbonate rocks that were deposited along the extensive Cordilleran miogeocline (Stewart and

Poole, 1972). Fractures, faults, and dissolution features provide the porosity and permeability that characterize the carbonate aquifer. Secondary aquifers exist in alluvial units and in Tertiary volcanic deposits. Confining units include the regional Proterozoic crystalline basement and most Proterozoic, Paleozoic, Mesozoic, and some Tertiary clastic rocks. The nature of connectivity between aquifers at different levels in the stratigraphic section is poorly known, as is the role of faults in providing conduits between adjacent basins. Faults juxtapose lithologic units of differing hydraulic properties, creating areas where aquifers are bounded laterally by confining units and where different aquifer systems may be hydraulically connected.

This study presents gravity and seismic interpretations of three basins in southern Nevada: Tule Desert, Meadow Valley Wash, and California Wash (Figure 1). For the purposes of this report, we define Meadow Valley Wash basin as the basin associated with the lower Meadow Valley Wash, between latitude 36°40'N and 37°20'N (Figure 1); the wash itself extends further to the north. Basic hydrologic and meteorological data of these three sparsely populated valleys are presented in Glancy and Van Denburgh (1969), Rush (1964), and Rush (1968), respectively. The study basins are within the southern portion of the White River groundwater flow system, which is contained within the larger Colorado groundwater flow system (Figure 1a, inset; Harrill and Prudic, 1998). Discharge from the White River groundwater flow system is primarily at springs (Figure 1a), especially the Muddy River Springs group that forms the Muddy River.

The northern portion of the study area is dominated by voluminous deposits of Miocene and Oligocene calc-alkaline volcanic rocks (Figure 1b) in the Clover, northern Meadow Valley, and Delamar Mountains that are associated with the Caliente and Kane Spring Wash caldera complexes (Figure 1a, inset; Rowley and others, 1995; Scott and others, 1995). The present-day topography of the study area is the product of Miocene basin-range extensional block faulting, structural doming, and strike-slip faulting that accommodates neighboring structural blocks with different extensional histories (Anderson and Barnhard, 1993; Page and others, 2005). Regionally, extensional faulting was most active between about 17 Ma and 8 Ma, and peak extension occurred on different faults at different times. For example, extension coupled with right slip on the Las Vegas Valley shear zone occurred primarily between ~14 Ma and ~8.5 Ma (Duebendorfer and Black, 1992; Duebendorfer and Simpson, 1994), and normal slip on the Piedmont fault, to the east of the study area at the boundary of the Great Basin and Colorado Plateau, was most active between 13 Ma and 10 Ma (Quigley and others, 2002). Within the study area, extension related to uplift of the Mormon Mountains occurred between 17 Ma and 14 Ma and was followed by moderate to steep tilting representing the main phase of extension (R.E. Anderson, written commun., 2005). Syntectonic and post-tectonic erosion and sedimentation produced the basin-fill deposits.

Anderson and Barnhard (1993) and Carpenter and Carpenter (1994) interpreted that primary extension in this area is accomplished along high-angle normal faults and strike slip faults. An alternative interpretation of the Cenozoic extension in this region involves large displacement, deeply rooted regional detachment faults that serve as the first order extensional structures (Wernicke and others, 1985; Axen and others, 1990). The nature of these detachments, whether long-lived faults that root into the mid-crust or the basal surfaces of slide blocks, has significant implications to the magnitude of crustal extension, with deep-rooted detachments accommodating large magnitudes of extension. Based on detailed investigation of the Mormon Peak detachment surface, Anders and others (2006) conclude that this structure was formed by numerous slide blocks, rather than by repeated slip on a long-lived and widespread fault surfaces.

To investigate the hydrogeologic framework of the basins in this area, numerous geophysical methods, including gravity, magnetics, and seismic reflection, have been applied in the past decade (e.g. Jachens and others, 1998; Phelps and others, 2000; Langenheim and others, 2000, 2001a, 2001b), and the present study builds on those techniques and results. Jachens and others (1998) interpret high-resolution aeromagnetic data of Tule Desert, the adjacent portion of Meadow Valley Wash basin, and much of the Virgin River depression. Langenheim and others (2001b) analyzed gravity, magnetics, and seismic observations in California Wash, including a short portion of one of the seismic reflection lines, LV-3, presented in this report.

Low-density, unconsolidated to semi-consolidated basin-fill deposits are juxtaposed against high-density bedrock units beneath many of the valleys, and this configuration produces significant gravity anomalies that can be used to infer the shape of the basins. Basin-fill deposits are often bedded, with seismic impedance contrasts that allow them to be imaged with seismic reflection surveys. By combining gravity analysis, which allows estimation of the volume of and shape of basin-fill deposits, with seismic reflection analysis, which illuminates the depositional and deformational architecture of these basins, we provide insights into the history and present configuration of these basins that complement insights from surface mapping.

Gravity Observations

In 2002, the U.S. Geological Survey (USGS) collected gravity observations at 344 sites (Appendix Table A1) to supplement the prior compilation of ~2500 stations in this area (Figure 1c; Kane and others, 1979; Snyder and others, 1981; Ponce, 1997, Langenheim and others, 1999; Langenheim and others, 2000). In April 2002, we collected 197 stations with locations determined using a Garmin hand-held Global Positioning System (GPS) receiver for longitude and latitude, and we used a Trimble AgGPS 132 to record elevations. Horizontal positions recorded with the Garmin hand-held unit have an uncertainty of 3-5 m. Vertical positions recorded with the Trimble AgGPS 132 have an uncertainty of less than 1.5 m. For some stations, benchmark and spot elevation control from USGS 7.5 minute series maps provided station elevations. In December 2002, we collected 147 stations with locations determined using a Trimble 4400 real-time kinematic (RTK) GPS unit to record longitude, latitude, and elevation at high precision, referenced to local GPS base stations surveyed-in with the National Geodetic Survey Online Positioning User Service (OPUS). Gravity station locations based on the Trimble RTK system typically have an error of 5-10 cm in the horizontal direction and 10-20 cm in the vertical direction. The gravity anomaly uncertainty at stations collected in April 2002 is about 0.5 mGal, primarily related to elevation uncertainty; the stations collected in December 2002 have a gravity uncertainty of <0.1 mGal due to the smaller elevation uncertainty. In April 2002, the gravity stations were collected in California Wash and Meadow Valley Wash (Figure 1c) and were named starting with MW or MV (Appendix Table A1); in December 2002, the gravity stations were collected from Tule Desert and surrounding ranges and named starting with TD.

Gravity data collected during April 2002 were tied to a gravity base station, GLEN, established at the Glendale Hotel in Glendale, Nev. GLEN has an observed gravity value of 979,682.63 mGal based on ties to LVGS, a gravity base station in front of the former U.S. Geological Survey office in Las Vegas, Nev. (observed gravity 979,593.62 mGal). Gravity data collected during December 2002 were tied to a gravity base station, MESC, established at the City Hall in Mesquite, Nev. MESC has an observed gravity value of 979,624.12 mGal, also based on ties to LVGS. All gravity data are referenced to the International Gravity Standardization Net of 1971 (IGSN 71) gravity datum (Morelli, 1974).

Values of observed gravity at the stations collected in 2002 were calculated by accounting for fluctuations related to tidal accelerations and for instrument drift constrained at the beginning and end of each field day. New gravity stations were collected within coverage gaps of the prior data and, where possible, in the ranges adjacent to the study basins. For both the prior and new gravity stations, we compared measured station elevations to interpolated elevations from USGS 30 m, and 10 m where available, digital elevation models (DEM). Where the station elevations differed by 80 feet (~24 m) or more from the DEM, the gravity station was omitted from further analysis; this occurred at 35 prior stations in the study area. In addition, we manually inspected and removed about 100 stations, including 4 collected in December 2002, where the station elevations differed by 40-80 feet (~12-24 m) from the interpolated DEM elevation.

We then calculated a series of predictable gravity effects for all of the stations to account for: the global gravity field, the reduction in gravity with increasing elevation (free-air correction), the effect of mass between the station and the geoid (simple Bouguer correction), the effect of the earth's curvature (curvature correction), the effect of topographic variation near the station (terrain correction), and the effect of compensating mass near the base of the crust (isostatic correction). The final gravity anomaly after application of these effects is termed the isostatic gravity anomaly and is useful for interpretation because it primarily reflects the density variations in the upper- and mid-crust (Simpson and others, 1986). For new gravity stations, estimates were made of the field terrain correction in a zone from the station out to a radius of 68 m; for the prior stations, this innermost terrain correction was not available. For all stations, digital terrain corrections beyond 68 m were calculated from DEMs in two stages: from 68 m to 2 km and from 2 km to 167 km using the algorithm of Plouff (1977). Other parameters that were used in the calculation of predictable gravity effects are typical for gravity studies in the Great Basin; these include an upper crustal density of 2.67 g/cm^3, a mantle-crust density contrast of 0.4 g/cm^3, and a nominal crustal thickness at sea level of 25 km. A typical maximum error of the new gravity stations is estimated to be ~0.5 mGal, and a typical maximum error of the prior gravity stations is estimated to be 0.5-1 mGal. In all cases, the errors are primarily due to elevation and terrain correction uncertainties, and they are small relative to the size of the gravity anomalies that arise from basin structures in the study area.

For some of the gravity analysis, isostatic gravity values from station data were gridded with a 500 m spacing, which is somewhat finer than the average station-spacing in the valleys (~2 km) and significantly finer that the spacing in the ranges, where gaps up to 10 km exist. During the gridding process, we identified a number of prior stations that had gravity values significantly different from their neighbors. To aid in identifying these noise spikes, we upward-continued (e.g., Blakely, 1996) the isostatic gravity field by 500 m, then calculated the difference between the original and upward-continued grids. This difference highlights short-wavelength anomalies in the grid, and thirty-eight gravity stations that contributed significant noise were identified and omitted from further analysis. All of the stations collected in 2002 passed this noise-editing test.

The isostatic gravity field of the study area (Figure 1d) reflects the major basin and range physiography: in general, positive isostatic anomalies are associated with the ranges and negative anomalies are associated with the basins. Areas with positive gravity anomalies have densities in the shallow-mid crust that are generally greater than the 2.67 g/cm^3 reduction density, and areas with negative gravity anomalies are associated with lower densities. The most positive anomalies, >20 mGal in Figure 1d, correspond to the western Mormon Mountains, the Virgin Mountains, and the South Virgin Mountains, where Precambrian crystalline basement occurs near the surface. The most negative anomalies, <30 mGal, occur beneath the Virgin River depression, where basin-fill deposits are among the thickest in the Great Basin Province (Saltus and Jachens, 1995; Bohannon and others, 1993; Langenheim and others, 2000, 2001a). The variable magnitudes of positive and negative isostatic gravity anomalies with other basins and ranges indicate that basement density varies across the study area and that basin-fill thickness and density vary among the basins. The exception to the correlation of positive anomalies with ranges occurs at the northern edge of the study area, north of 37°10'N, where negative anomalies predominate due to thick accumulations of low-density volcanic deposits near the Caliente and Kane Spring Wash caldera complexes (Figure 1a, inset). This northern edge of study area lies at the southern limit of a regional, 90 mGal Bouguer gravity anomaly low identified by Eaton and others (1978). Eaton and others (1978) interpret this anomaly as arising from a number of factors characteristic of this portion of the western Cordillera: lateral temperature variations in the crust and lithosphere, Cenozoic intrusions, and variable metamorphism and extension across the Great Basin. By utilizing the isostatic gravity anomaly and by endeavoring to separate anomaly contributions of basin-fill material from other low-density rocks, we focus our gravity analysis on the basin development of this area, rather than the regional trends exemplified by Eaton and others (1978).

Gravity Analysis

Isostatic gravity anomalies were analyzed in several modes: first, a grid-based inversion technique was used to estimate the depth variation of Cenozoic basins across the study area (Jachens and Moring, 1990); second, a grid-based match filtering analysis (Syberg, 1972) separated gravity anomalies generated by shallower sources from those derived from deeper sources in Tule Desert; and third, a forward-model technique (Talwani and others, 1959) was used to analyze gravity variations along one of the seismic reflection lines.

The "depth-to-basement" inversion technique endeavors (1) to separate contributions to the isostatic gravity anomaly that arise from Cenozoic sedimentary and volcanic deposits and those from pre-Cenozoic rocks and (2) to convert the low-density contributions from the young deposits into a model of basin depth (Jachens and Moring, 1990). This is an inverse geophysical approach because it solves for model geometry based on observations of gravity, constrained by outcrop patterns and by *a priori* assumptions about the density contrast of basin fill relative to surrounding rocks. This method is iterative and has been successfully applied to the entire Great Basin (Saltus and Jachens, 1995) and to individual basins and groups of basins in southern Nevada (e.g., Langenheim and others, 2001b). The depth-to-basement method first separates those gravity stations that lie on Cenozoic deposits (termed "basin") from those that lie on pre-Cenozoic rocks. These pre-Cenozoic units are defined as "basement", a usage that differs from a common description of old, crystalline rocks as basement in many areas. The isostatic gravity anomalies at basement stations are then interpolated across the intervening basins, and differences between the interpolated basement gravity values and those measured at basin stations are attributed to the low-density basin fill. Using a 1-D approximation, the depth of the basin fill is estimated from the size of the basin gravity anomaly at each grid point, and then the gravitational attraction of these interpreted basins is calculated. Where a basement gravity station lies close to basin material, some of the attraction of the low-density fill will influence its gravity value; thus, the calculated basin attraction must be removed from the gravity value at each basement station. This process yields estimates of basement gravity, basin gravity, and depth to basement beneath the basins. This sequence is then repeated for multiple iterations with successively refined basement gravity estimates, until the estimates of basin depth converge.

In this study, gravity stations are classified by their placement on three geological units: pre-Cenozoic basement, Cenozoic sedimentary fill, and Cenozoic volcanic deposits. The distribution of these units is based on the 1:250,000 geologic map of Page and others (2005). The depth of the resulting basement surface is assumed to be the thickness of sedimentary deposits where sediments are at the surface and to be the thickness of volcanic deposits where volcanics crop out. This assumption of the depth-to-basement technique is a simplification because sediments overlie volcanic deposits in some areas and they are interbedded in other areas.

A critical input to the depth-to-basement method is the depth variation of the density contrast of basin fill material relative to surrounding basement. This density profile is the link that allows conversion of basin gravity anomalies to basin depth estimates. Measured density-depth functions are available from deep boreholes in other parts of the Great Basin (e.g. Healey and others, 1984) but not from the study area. We tested a number of density-depth functions in our calculations, including those used in Jachens and Moring (1990) that were deemed appropriate for the entire Great Basin (Table 1). After some experimentation, we adopted the density-depth relationship termed Model B in Langenheim and others (2001b), derived from seismic velocity analysis of reflection profile LV-1 across California Wash. This density-depth function (Table 1) has smaller density contrasts than that of Jachens and Moring (1990), leading to deeper estimated basins that better matched independent seismic constraints on basement depths. In these density-depth functions, density increases with depth, especially within the uppermost 600 m. Near the surface, sedimentary deposits are assumed to be less dense than the volcanic deposits; deeper than 600 m, the density-depth functions are similar. This correspondence in density makes it difficult to separate the geophysical effects of sedimentary and volcanic deposits using gravity methods in this area. That said, where surface exposure changes from sedimentary to volcanic deposits, the differing density-depth functions can yield steps in the basement depth estimate that are artifacts of the method due to the assumption that the contact between volcanic and sedimentary deposits is vertical from the surface to the basement. An example of such an artifact is described below in the section presenting results from northern Meadow Valley Wash basin.

In the depth-to-basement technique, independently measured depths to the base of Cenozoic deposits can be used as important constraints to the basin depth estimation. These measurements are available typically from deep boreholes and from seismic reflection observations. In the study area, there are about a dozen wells drilled for oil and gas exploration (Hess, 2004), and there are three large-diameter wells drilled from the MX missile project (Figure 1a; Bunch and Harrill, 1984). Three deep oil and gas wells with downhole lithologic information lie within the study area (Hess, 2004): Texaco Federal #1 in the southern Meadow Valley Mountains, Grace Petroleum Arrow Canyon #1 in the southern Arrow Canyon Range, and Mobil Virgin River #1 in southern Mormon Mesa. The downhole lithology and structural information can aid in interpreting the subsurface geological configuration of this area (e.g. Page and others, 2006). Only the Mobil Virgin River #1 well lies atop a significant thickness of Cenozoic basin fill, so only that well is useful in providing an independent constraint to the gravity depth-to-basement solution. Migrated and depth-converted seismic reflection observations may be used to constrain depth-to-basement solutions where a clear boundary between Cenozoic and pre-Cenozoic units is observed. Independent basement depth constraints may be applied to the modeling using two approaches: either as *a priori* exact and minimum depth constraints that must be satisfied as the depth-to-basement algorithm iterates, or as post-modeling validation of the depth-to-basement solution. Deciding on which approach to use depends on the distribution of depth constraints and on the availability of measured density-depth functions in the study area. In this study, we utilize sparse depth estimates from seismic and well constraints using the second approach, to validate the density-depth function utilized in the depth-to-basement solution.

The second mode of gravity analysis utilizes match filtering, where the power spectrum of a gravity field is used to separate anomalies arising from different depths in the earth (Syberg, 1972). This technique is especially helpful in Tule Desert, where volcanic rocks of the adjacent Clover Mountains have densities that are similar to the low densities of basin fill material and where the depth-to-basement technique cannot differentiate between volumes of volcanic versus sedimentary deposits. As discussed below, match filtering allows an objective separation of those gravity anomalie. The longer-wavelength gravity anomalies are most likely related to the transition of pre-Cenozoic basement and thick volcanic deposits from those gravity anomalies, and the shorter-wavelength anomalies most likely reflect the thickness variations of Tule Desert basin fill.

In addition to the grid-based analyses, we conducted two-dimensional forward modeling of the gravity anomalies along seismic reflection line LV-6, which crosses Meadow Valley Wash and Tule Desert basins approximately perpendicular to the strike of regional geologic structures (Figure 1b). In this method, we construct models of subsurface geological units having specified densities, modifying the corners of the blocks and the densities so that the calculated gravity values match the observed isostatic gravity anomalies at stations collected along the seismic line. This analysis assumes that geologic structures are aligned nearly perpendicular to the model profile and that, in the case presented below, geological bodies extend a great distance (relative to their along-profile dimension) away from the plane of the profile. Because no other seismic line of this study is suitably oriented with respect to regional geologic structures, we applied this method only to LV-6. In addition to the constraint of matching observed gravity anomalies, we also incorporate model constraints from outcrop geology and from two water wells, MW3 and MW2 (Figure 2a), drilled for monitoring purposes near line LV-6 in Tule Desert (HydroSystems, Inc., 2002). In MW3, alluvium was found in the upper 250 m, below which was 390 m of Tertiary volcanic rocks to the base of the hole. In MW2, 366 m of alluvium was drilled before reaching pre-Cenozoic carbonate rocks at the floor of the basin.

Rock Samples

At 20 gravity stations situated on outcrop, we collected 32 rock hand-samples (Appendix Table A2) to measure their density (Johnson and Olhoeft, 1984) and magnetic susceptibility properties in the lab. These rock properties supplemented those of ~200 other rocks from prior studies, and they were used to guide the gravity modeling. Rock property measurements from all of the samples are summarized in Table 2 as averages grouped by rock type. While physical properties of hand-samples may not individually represent well the bulk properties of *in situ* volumes of rock, especially those at depth, the measurements can aid in establishing realistic density variations among the lithologic units in the gravity modeling. Except for the felsic volcanic and clastic sedimentary rocks, all of the other rock types (Table 2) have saturated bulk densities statistically equal to or greater than the 2.67 g/cm^3 value utilized for reducing the gravity anomalies; thus, isostatic gravity anomalies over basement exposures are generally positive (Figure 1d). Pre-Cenozoic clastic sedimentary rocks are relatively uncommon across the study area, and felsic volcanic rocks dominate the northern portion of the study area in the Clover, Delamar, and northern Meadow Valley Mountains. The strong negative isostatic gravity anomalies around the Caliente caldera complex and neighboring volcanic centers reflect the thick accumulations of dominantly silicic ash flow tuffs and lava flows and their subjacent plutons in this area. The low and variable densities of the volcanic units are similar to *in situ* densities measured in young basin-fill deposits, and thus gravity observations are not effective at distinguishing between accumulations of sediments and these volcanic deposits.

Seismic Reflection Lines

Multichannel seismic reflection lines (Figure 1c) were shot in 1978-1980 by Pacific West Exploration Co., and the data were acquired by the USGS with limited publication rights. In this study, we display results from lines LV-6 across Tule Desert and northern Meadow Valley Wash, LV-3 along the axes of Meadow Valley Wash and California Wash, and LV-2A across a portion of southern Meadow Valley Wash basin (Figure 1c). Other seismic reflection data in this area include a number of additional “LV” lines, both in California Wash (LV-1 and LV-1Aext shown in Langenheim and others, 2001b) and a network of “LV” and other lines in the Virgin River depression (Bohannon and others, 1993) to the east of the study valleys. In addition, three industry seismic reflection lines were displayed and interpreted by Carpenter and Carpenter (1994), one of which was nearly coincident with LV-6 where they cross Tule Desert. Carpenter and Carpenter’s (1994) structural interpretations were aided by additional proprietary industry seismic reflection data that were not illustrated in their study.

LV-6 and LV-3 were shot with explosive Primacord, and LV-2A was shot using reverberative Vibroseis (18s, 12-48 Hz sweep) energy sources. All three lines were recorded to 6 seconds on 48 channels with a nominal fold of 24 and with a geophone spacing of 67 m. Data processing consisted of a standardized sequence of: automatic gain control scaling, single design window spiking deconvolution, velocity analysis, surface-consistent residual statics, a second velocity analysis, normal move-out and stack, shift to a constant datum, migration using a smoothed stacking velocity field, bandpass filter at 10-50 Hz, automatic gain control scaling, second-zero-crossing predictive deconvolution, and frequency-space deconvolution. Because of the 201 m separation between the shots and the nearest geophone, the seismic sections do not image the shallowest 100-200 m of the subsurface (Figures 3-8). LV-2A is relatively short, ~10.5 km long, with a 2-km-wide data gap in its western half (Figure 6). The presence of this data gap reduces the quality of the adjacent seismic imaging by reducing the fold, and it makes uncertain the correlations of reflectors between the eastern and western portions of the line.

Bohannon and others (1993) developed a seismic stratigraphic framework to interpret seismic reflectors in the Virgin River depression, directly east of the present study area, based on analysis of the lithologic and sonic logs of the Mobil Virgin River #1A oil exploration well situated on Mormon Mesa (Figure 1a). This well penetrated a ~2-km-thick sequence of Tertiary basin fill, primarily the Muddy Creek and Horse Spring Formations, which overlies sedimentary rocks of Cretaceous age and a sequence of Triassic to Cambrian sedimentary rocks. This Phanerozoic package rests on Proterozoic crystalline basement at ~5.8 km depth in Mobil Virgin River #1A. Based on sonic velocity contrasts, Bohannon and others (1993) calculated synthetic seismograms for the frequency band of the observed reflection data, and they assigned reflector characteristics (strongly-reflective, weakly-reflective, and non-reflective) to eight subdivisions of the stratigraphic sequence penetrated by the well. Using these guidelines, Bohannon and others (1993) map stratigraphic contacts and fault locations throughout the Virgin River depression, and they infer that three phases of middle Tertiary extension and subsidence generated the present-day basin structure.

In the seismic stratigraphy of Bohannon and others (1993), the strongest reflectors are present in several members of the Tertiary section that are separated by seismically less-reflective sections. Moderate-strength reflectors are present in some of the Mesozoic and Paleozoic rocks, but in general, reflectors are weaker in the pre-Cenozoic section than in the Cenozoic section.

There are no deep oil wells that penetrate the Phanerozoic section in the study area, so development of a seismic stratigraphy as was done at the Mobil Virgin River #1A well is not possible. Because many of the Tertiary and pre-Tertiary units are similar between California and Meadow Valley Washes and the Virgin River depression, we interpreted the reflectors using a generalized form of the Bohannon and others (1993) seismic stratigraphy. For this study, we divide the reflectors into two groups: shallow, strong, laminar, continuous packages that we infer are of Cenozoic sedimentary units, and deeper, weaker, and less-continuous packages that we infer are of Mesozoic and older rocks. Of all of the seismic reflection lines in the study area and in the Virgin River depression, only a small segment of LV-6 crosses Cenozoic volcanic outcrop; in that segment, there are no clear features in the shallow section that can be attributable to volcanic rocks. An important similarity between the seismic lines of this study and those of Bohannon and others (1993) is that the degree of deformation of Tertiary units increases with depth in the section, reflecting the change from pre- and syntectonic deposition at deeper levels of the valley fill to post-tectonic deposition near the land-surface.

We observe that the strength and continuity of seismic reflectors correlate with surface geology and topography, suggesting that near-surface conditions affect the imaging quality of the seismic reflection data in the study basins. For example, across the young, fine-grained surficial deposits of California Wash Valley, reflectors are strong, of uniform quality, and continuous (Figure 7). In contrast, northward along the drainage of Meadow Valley Wash, reflector quality throughout the section is degraded (Figure 4) as the wash has incised older, coarser-grained, and more deformed units and as the topography becomes rougher. This behavior, described more fully in the Appendix, limits our ability to interpret some areas that have low levels of seismic reflectivity.

Seismic reflection interpretations were guided by outcrop geology near the seismic lines, by wells near the lines that have lithologic information, and by structures inferred from gravity analysis. For the most part, faults were identified where they truncate and offset subhorizontal reflectors, and their apparent dip angles in the plane of the seismic profiles are poorly constrained because the plane of the fault is not imaged. In one instance, however, a clear fault-plane reflector was observed from a low-angle fault. Folds and unconformities were often observed in the vicinity of faults in the seismic reflection sections.

Results

Tule Desert

The ranges bounding Tule Desert lie at the transition between those comprised of high density basement to the south and those comprised of medium and low density volcanic rocks to the north, as reflected in geology (Figure 1b) and gravity (Figure 1d). The saturated bulk densities of four felsic volcanic samples from the Clover Mountains range from 2.0 to 2.3 g/cm^3 (Table A2), values that are indistinguishable from typical densities of sedimentary fill. While the bulk density of the Clover Mountains is higher than these hand-sample values because the range is predominantly composed of andesite and densely-welded rhyolite tuffs, the depth-to-basement technique is not well-suited to define the shape of Tule Desert sedimentary basin because the density contrasts between alluvial infill and adjacent Clover Mountain rock are small. However, we can exploit the different wavelength characteristics of gravity anomalies that arise from the shallow and deep density variations below Tule Desert to help characterize their sources. By delineating straight-line portions of the power spectrum of the isostatic gravity anomaly using the match filter technique (Syberg, 1972), we separate the gravity anomaly into deep-source and shallow-source contributions (Figures 2c and 2d, respectively).

The deep-source contribution (Figure 2c) illustrates that long-wavelength gravity anomalies, and thus densities, mimic closely the regional geological configuration: 1) high densities occur at the core of the Mormon Mountains where dense Proterozoic basement is shallow, 2) the area of high density extends to the Tule Springs Hills, 3) low densities are present beneath the volcanic rocks of Clover Mountains to the north, and 4) low densities track the thickening sedimentary deposits into the Virgin River depression to the southeast. Features of the deep-source gravity anomaly are uncorrelated with the outline of Tule Desert (Figure 2c).

In contrast, the shallow-source gravity anomaly (Figure 2d) shows poor correlation with the regional geology. Basins are associated both with gravity highs and lows, and ranges generally have weak gravity anomalies. That said, correlations between local geology and shallow-source gravity anomalies do exist. For instance, the two outcrops of Mesozoic and Paleozoic sedimentary rocks in the southern Clover Mountains to the northwest and northeast of Tule Desert (Figure 2b) are correlated with small positive gravity anomalies in Figure 2d. These outcrops are likely not volumetrically significant, however, because they do not have a signature in the deeper-source anomaly. In addition, the shallow-source gravity field contains a number of distinct anomalies that are confined to the outline of Tule Desert: a low in the northeast corner and two lows separated by a northeast-trending gravity high near the center of the basin. This mid-basin gravity high correlates spatially with the isolated outcrops of Paleozoic sedimentary rocks in the Clover Mountains northwest of Tule Desert and with the isolated outcrop of Paleozoic rocks just southwest of TDW well (Figure 2b) that extends north from the Mormon Mountains into Tule Desert. This gravity anomaly likely reflects an intrabasin basement horst block, a feature substantiated by a magnetotelluric survey in Tule Desert (Zonge Engineering and Research Organization, Inc., 2002). The match filter gravity analysis, while effective at identifying anomalies that arise from density variations at different depths, does not lend itself to precise estimates of basement depths. The depth-to-basement model (Figure 1e) exhibits results that are broadly consistent with those of the match filter analysis. However, we view that the estimated basin depth values are uncertain because the method does not allow for sedimentary basin-fill units to overlie volcanic units, and thus we develop a forward model of the density configuration, described below.

Seismic reflection line LV-6 (Figure 3) crosses the widest portion of Tule Desert (Figure 2a) and provides an image of the subsurface that is complementary to what can be inferred from gravity. The eastern half of the Tule Desert is underlain by several clear, horizontal reflections situated 1-3 km below the surface (Figure 3 at profile distances of 16-22 km). We interpret these as reflections from pre-Cenozoic strata rather than Cenozoic basin-fill because water wells in Tule Desert (Figures 2 and 3b) that penetrate the alluvial section encounter pre-Cenozoic rocks within 400 m of the surface (HydroSystems, Inc., 2002). HydroSystems, Inc. (2002) reported that MW2 penetrated Triassic rocks at 366 m depth, and Page and others (2006) interpret in their cross-section A-A' that Triassic and lower Permian units lie immediately beneath Tule Desert basin. Thus, the reflectors beneath the eastern half of Tule Desert likely arise from Triassic and upper Paleozoic rocks, whose nearest surface exposure is in the Tule Springs Hills just to the east of the seismic profile. For such a shallow basin, the base of the alluvium is not well imaged using the seismic reflection acquisition parameters of LV-6 (Figure 3b). Towards the east where the line crosses the northern Tule Springs Hills, the reflectors are less continuous and have significant dip. We interpret these disruptions to represent deformation resulting from movement on steep faults at the eastern margin of Tule Desert basin (Figure 3b, kilometers 21 to 26). The largest of these faults corresponds to the East Tule Desert fault (Figure 2b; Axen and others, 1990; Anderson and Barnhard, 1993; Hintze and Axen, 2001). While normal-sense offset is consistent with the seismic reflector geometry, significant strike-slip motion has also been reported on the East Tule Desert fault (Hintze and Axen, 2001).

A complementary geophysical view of the subsurface is provided by aeromagnetic anomalies (Figure 2e). Jachens and others (1998) analyzed a detailed aeromagnetic survey that included Tule Desert and the adjacent Meadow Valley Wash basin. To characterize the shallow subsurface, they filtered the aeromagnetic anomalies to emphasize shallow magnetic contrasts and they identified the locations of maximum horizontal gradients of the high-resolution magnetic field (Blakely and Simpson, 1986). The calculation of these high-resolution aeromagnetic anomalies is described in the Appendix of Jachens and others (1998), and these anomalies are used to identify past drainage channels where magnetic minerals were preferentially deposited and to identify where shallow, magnetic volcanic deposits are buried. In the high-resolution aeromagnetic field, lineaments of maximum horizontal gradient positions lie within Tule Desert, near and parallel to its eastern margin (Figure 2e). These types of lineaments are often produced by faults that juxtapose rocks of differing magnetic properties, and the placement of these lineaments is consistent with the location of the East Tule Desert fault, inferred from geology and geophysics, a few kilometers west of the Tule Springs Hills. In addition to aiding the detection of buried faults, the high-resolution aeromagnetic anomaly shows the location of exposed and shallowly-buried volcanic rocks in the Clover Mountains and adjacent areas. The high magnitude and short wavelength of these anomalies indicate that the volcanic units are generally magnetic, but heterogeneous at short scales, consistent with hand-sample measurements of susceptibility (Tables 2 and A2).

In the center of Tule Desert (Figure 3b, kilometers 13 to 15), two faults of opposing dip are inferred to account for disruptions in the 1-3 km deep reflectors, although their dips and magnitudes of offset are poorly constrained by the seismic data. The two faults, as envisioned, create a small horst block that is consistent with the location of the inferred intrabasin high from the match filtering analysis (Figure 2d) and from a controlled source audiofrequency magnetotelluric (CSAMT) study (Zonge Engineering and Research Organization, Inc., 2002). Several CSAMT lines that cross this feature sense a shallow, high resistivity block (Zonge Engineering and Research Organization, Inc., 2002). The authors of this report note the correspondence of this “central resistive block” in the shallow subsurface with the local high in isostatic gravity anomaly, and they suggest, as we do, that it arises from a small horst of resistive carbonate basement above which the alluvial section is thin. The basement high does not appear to juxtapose units with different magnetic properties because high-resolution aeromagnetic anomalies do not correlate with its position (Figure 2e; Jachens and others, 1998).

Beneath the western portion of Tule Desert (Figure 3b, kilometers 8 to 12), no coherent seismic reflectors are observed. In this area, volcanic rocks crop out in the small north-south ridge between the Mormon Mountains and the Clover Mountains, and water well MW3 encountered volcanic rocks at 250 m depth (HydroSystems, Inc., 2002). The absence of coherent reflectors suggests either that these Tertiary volcanic rocks are seismically transparent and thick, or that they attenuate the seismic energy such that deeper reflectors are not imaged. From interpretive geologic cross-section analysis (A-A’ of Page and others, 2006), the volcanic layer is thought to be thin (<500 m) beneath western Tule Desert, arguing that the second explanation of higher seismic attenuation is preferred. Carpenter and Carpenter (1994) interpreted a thick (>1 km) volcanic section across the entire Tule Desert basin, with a greatest thickness in the east, from their seismic reflection line 5-5A. In contrast, Page and others (2006) interpreted the volcanic rocks to be thin beneath western Tule Desert, based partly on the fact that volcanic rocks are absent in the subsurface below eastern Tule Desert as demonstrated by drill hole data. HydroSystems, Inc. (2002) report alluvial thicknesses of 256 m at well MW1 and 366 m at MW2 (Figure 2a), directly overlying carbonate rocks of the regional aquifer system. The absence of volcanic rocks in eastern Tule Desert indicates these rocks pinch out from west to east across the basin. In addition, the Tertiary volcanic section may be abbreviated in western Tule Desert near the northern Mormon Mountains, because of missing volcanic units (R.E. Anderson, written commun., 2003). Jachens and others (1998) suggest that a group of NW-SE-trending faults underlies southern and western Tule Desert basin, perhaps as extensions of faults exposed in volcanic units of the Caliente caldera complex. These proposed buried faults cannot be evaluated using LV-6 because seismic reflectors are not observed on LV-6 beneath western Tule Desert.

To quantify the basin depth variations that can explain both the gravity and seismic observations, we constructed a two-dimensional model of density structure beneath LV-6 (Figure 3d), assuming three geologic units: Quaternary and Tertiary undifferentiated sediments (QTu), Tertiary volcanic rocks (Tv), and pre-Cenozoic basement (pre-Cz). These units are constrained to match the surface geological exposure and the alluvial thicknesses at water wells MW3 and MW2. In the modeling process, densities and block locations were varied manually to achieve as good a match as possible of the predicted gravity anomaly to the observed anomaly (Figure 3c), while maintaining densities consistent with measured values and block boundaries consistent with surface geology and the down-hole constraints from the water wells. The significant results of this modeling are that Cenozoic basin fill deposits in Tule Desert basin, where crossed by LV-6, are nowhere thicker than 500 m and that the intrabasin high has a height of 100-200 m. By extrapolating the basin thickness beneath LV-6 to the rest of Tule Desert basin using the shallow-source gravity anomaly (Figure 2d), we infer that the Cenozoic basin-fill deposits are thickest at the northeastern portion of Tule Desert, where they have a thickness of 1.5-2 km.

Meadow Valley Wash

Gravity and seismic reflection data indicate that Meadow Valley Wash contains three subbasins that are separated by buried basement highs (Figure 1e): the northern subbasin extends northwards from a point ~5 km south of Carp; the central subbasin lies between Galt and Rox, and the southern subbasin lies between Rox and Moapa. The ranges bordering the northern portion of Meadow Valley Wash basin consist mainly of volcanic rocks of the northern Meadow Valley Mountains and the Clover Mountains (Figures 1a,1b), where the isostatic gravity anomaly transitions from positive values in the south to negative values in the north (Figure 1d). The depth-to-basement solution (Figure 1e) indicates thick Cenozoic sedimentary and volcanic deposits in the northern subbasin. However, as with Tule Desert, this technique cannot differentiate the low-density sedimentary from volcanic sources. The rapid deepening of the basin north of Carp, Nev., is an artifact of the change in basin-fill material, and thus density-depth function, from predominantly sedimentary units in the south to volcanic units in the north. While the volcanic units are likely to be quite thick in the vicinity of the Kane Spring Wash caldera and the Caliente caldera complex (Figure 1a, inset), the nature of the caldera boundaries is not well-recovered by the depth-to-basement gravity inversion method.

In the seismic reflection profiles, both the western portions of LV-6 (Figure 3) and the northern portions of LV-3 (Figure 4) exhibit strong dipping reflectors within the uppermost 3 km. LV-6 is perpendicular to the main structures, and the disrupted reflectors indicate a series of normal faults at the eastern margin of Meadow Valley Wash basin (Figure 3). These faults correspond to the Meadow Valley Wash fault zone (Figure 2b; Page and others, 2005, 2006) that forms the eastern boundary of Meadow Valley Wash basin. In LV-3 north of Carp, Nev., reflectors dip to the north, suggesting thick basin-fill deposits that have a reflective sequence at their base (Figure 4).

In the gravity model (Figure 3d) along LV-6, we match the gravity anomaly at the eastern margin of Meadow Valley Wash basin with a ~1.5 km normal dip-offset on the easternmost basin-bounding fault inferred from LV-6 (Figure 3b) that corresponds with the Meadow Valley Wash Fault. Because of the similarity in density of the sedimentary and volcanic basin-fill deposits and because these deposits are often interbedded, our modeling cannot place hard constraints on their relative thicknesses beneath Meadow Valley Wash. In our final model, we include a volcanic layer that gradually thins eastward from the Meadow Valley Mountains, ultimately pinching out near the small, buried ridge in the center of Tule Desert (Figure 3d).

About 5 km south of Carp, Nev., the ranges surrounding Meadow Valley Wash are comprised of Paleozoic sedimentary rocks, and the wash crosses exposed Mississippian-Permian Bird Spring Formation that forms a basement high near Galt, Nev. (Figure 1b). Thus, the depth-to-basement map of Meadow Valley Wash basin south of Carp, Nev., is likely to reflect variations in thickness of alluvium rather than reflecting a combined thickness of alluvial and volcanic deposits. South of Galt, two subbasins are present (Figure 1e): the central one between the Bird Spring Formation exposure along the wash and Rox, Nev., and the southern one between Rox and the southern end of Meadow Valley Wash at the Muddy River. A small outcrop of Permian Kaibab Formation at Rox (Figure 1b) marks a basement high that separates the central and southern subbasins of Meadow Valley Wash basin.

The central subbasin between Galt and Rox is somewhat smaller and shallower than its southern counterpart (Figure 1e). Using the density-depth function determined from this area, the maximum depth of the central subbasin is slightly more than 2 km, and the maximum depth of the southern subbasin is slightly more than 3 km, and the intrabasin divide is everywhere shallower than 500 m below the land surface.

The division of Meadow Valley Wash into two subbasins south of Galt, Nev., is well illustrated in seismic reflection line LV-3 (Figures 4 and 5). North of Rox, LV-3 crosses the southeastern portion of the central subbasin

(Figures 4 and 5, kilometers 15 to 23), where the laminated reflector sequence extends to a maximum depth of about 1.5 km. Water well Rox-MW-1 lies about 2 km north of the outcrop of Kaibab Formation near Rox, and it bottomed in alluvium at 725 m depth. The lateral boundaries of the central subbasin along LV-3 are not clear from the seismic reflection image; the base of the Cenozoic section is drawn as a continuous line, but faults observed in the reflection section may play a role in governing the basin geometry. No such faults have been recognized in surficial geological mapping (Page and others, 2005).

LV-3 is located just west of the subsurface axis of the southern subbasin of Meadow Valley Wash. The southern subbasin (Figure 5, kilometers -15 to 12) extends nearly 4 km below LV-3, and reflectors near the lateral margins suggest a significant role for faulting in the development of the basin. South of Rox, at least two faults drop down the basin to a near-constant depth, which gradually shoals towards the southern end of the subbasin with an interruption by one fault (Figure 5, kilometer -15). Near the southern end of the subbasin, water well EH-2B encountered the top of basement at a depth of 1.2 km (D.L. Schmidt, oral commun., 2003), a constraint that is consistent with our interpretation of the seismic reflection profile. South of Rox, a number of faults with a variety of orientations have been mapped in Pliocene and older deposits (Page and others, 2005; Figure 1b), indicating that the southern subbasin is complexly deformed. This deformation is also illustrated by seismic reflectors within the basin-fill material of the southern subbasin that have the form of a broad anticline centered at kilometer 2 (Figure 5), with synforms on either side, especially in the deeper portion of the basin. Small angular unconformities are also present in the basin-fill material. The three-dimensional shape of these folds cannot be determined from LV-3 alone, but the perpendicular seismic line LV-2A (Figure 6) shows strong reflectors with a range of subhorizontal dips in the lower basin-fill portion where the line crosses LV-3.

About 2 km south of Rox, a number of subhorizontal reflectors occur between 1 km and 4 km below sea-level (Figure 4). We interpret these reflectors as being situated below the floor of the basin because they are deep and laterally in close proximity to surface outcrop just north of Rox and because they do not have the laterally continuous character of the reflectors in the adjacent subbasins. From cross-section C-C’ of Page and others (2006), these deep reflections likely arise from Mesozoic and Paleozoic units. Reflections from below the interpreted Cenozoic sequence are sparse elsewhere along LV-3 in Meadow Valley Wash (Figures 4 and 5).

The short seismic reflection line LV-2A (Figure 6) presents a structure-perpendicular view of southern Meadow Valley Wash basin that is complementary to that provided by LV-3. The most striking feature is the prominent, low angle, west dipping reflector that is strongest between kilometers 4 and 9 (Figure 6). Where the reflector is straightest in the migrated section, it has a dip of 20° ± 2°, and it appears to flatten towards both of its ends. The data gap between 2.3 km and 4.2 km prevents a clear correlation of this reflector to the western segment of the line, and because of its short length, the seismic migration is least reliable in that western segment (Figure 6). On LV-3, which crosses LV-2A at kilometer 0, the base of the Cenozoic section is interpreted to be ~3.5 km below sea level (Figure 5). If the strong, dipping reflector has a constant dip westward across the data gap, then it would intersect the LV-3 crossing at near the base of the interpreted Cenozoic section. More likely, the shoaling dip at profile distances <5 km is real, in which case the reflector would project at a level within the Cenozoic basin fill. In the up-dip direction, the reflector projects to the land surface at a position near kilometer 13 (that is, 3 km east of the eastern limit of LV-2A) if extended linearly at a constant 20° angle. This position is close to the small ridge of Paleozoic rocks that extends southwards from the Mormon Mountains (Figure 1b). Alternatively, if the dip of the reflector flattens as is suggested by its character between kilometers 8 and 9 (Figure 6), then its intersection with the land surface would be significantly to the east of the ridge.

A number of distinctive reflector patterns are associated with the low-angle reflector (Figure 6). Overlying reflectors appear both to lap onto the prominent reflector (kilometer 5) and to be truncated against it (kilometer 7). An antiform, flanked by small synforms, marks the reflector package that is truncated. Above this package is an apparent, broader antiform with an axis near kilometer 7.

We interpret the prominent low-angle reflector in seismic line LV-2A as a low-angle normal fault at or near the base of Cenozoic basin-fill deposits. Carpenter and Carpenter (1994) noted similar low angle features in their seismic line 6, about 12 km to the south of LV-2A, and they interpreted these features as ecoulements, or gravity slide slip surfaces, at the Cenozoic basin-fill/Pre-Cenozoic bedrock interface. In Carpenter and Carpenter’s (1994) analysis of seismic line 6, interpreted basin fill deposits above the proposed fault are highly deformed, and have a strikingly similar folded style to deformed Cenozoic basin-fill deposits in LV-2A (Figure 6). We agree with Carpenter and Carpenter’s (1994) interpretation of a gravity-slide fault at the base of deformed basin fill deposits in Lower Meadow Valley Wash. Furthermore because the same feature is imaged in LV-2A, we interpret that this fault underlies much of the southern subbasin of Meadow Valley Wash and that it may have been a significant structure accommodating the extensional development of the basin. The explanation of this reflector as a low angle gravity-slide fault at or near the base of the basin-fill units is supported by a number of factors: a) Isostatic gravity (Figure 1d) and modeled basin depth (Figure 1e) indicate that the basin is relatively thick along LV-2A; b) the strength and continuity of reflectors above the fault plane, and even below the fault plane, are more similar to basin-fill reflectors than they are to basement units in this area; and c) this low-angle reflector has a similar character to intra-basin-fill normal faults interpreted immediately to the east in the Virgin River depression (Bohannon and others, 1993, seismic line LV-2). Our interpretations of LV-2A are consistent with the model of Anders and others (2006) of the western flank of the Mormon Mountains as a series of distinct slide blocks with differing orientations (Anders and others, 2006, figure 5b). The variable dips in LV-2A reflectors above the prominent reflector between profile distances of 5-7 km may arise from slide blocks, and in this case, significant post-slide deposition would have buried these blocks beneath 1-2 km of alluvium.

California Wash

The isostatic gravity anomaly of California Wash basin indicates that it is a single structural depression (Figure 1d). Based on the density-depth function assumed for this study, the depth-to-basement solution suggests that the basin reaches a maximum thickness of 3 km near its center (Figure 1e). Seismic reflection line LV-3 is subparallel to the axis of the basin and images a thick sequence of laminar reflectors along the entire basin (Figure 7). At its deepest (Figure 7, kilometer -32), the basin reaches almost 4 km depth. Near that location, a warping of the lower two-thirds of the Cenozoic basin-fill reflector sequence suggests the presence of a buried normal fault that deforms the older Tertiary basin-fill deposits and offsets both the basin-fill and underlying Paleozoic bedrock. This fault may be hydrologically significant because it represents connectivity between the basin-fill and carbonate aquifer systems. Langenheim and others (2001b) identify an unconformity in seismic line LV-1, which is perpendicular to the basin and which crosses LV-3 at kilometer -35 (Figure 7), and they suggest that this unconformity may mark the division between the Miocene Muddy Creek Formation above and the Miocene Horse Springs Formation below. The unconformity, at 0.5 km below sea level where LV-1 crosses LV-3, is not as evident in the along-strike LV-3 line as in LV-1, but this is the level at which the offset and warping of reflectors by the buried fault near the center of the basin is diminished.

Disruptions and offsets in the reflectors also suggest the presence of faults at the southern and, especially, northern margins of California Wash basin (Figure 7b, kilometer -45 and kilometers -20 to -16). At the northern end of California Wash, exposed and concealed faults have been recognized in geological mapping (Figure 1b, Page and others, 2005), and the locations of some of these faults correlate with the faults interpreted from the seismic section. Near the southern end of LV-3, the fault interpreted at kilometer -45 correlates with down-to-the-east normal faults mapped by Page and other (2005). The dip of faults interpreted from the seismic line may be shallower than true dips because of the oblique intersection between the fault and seismic profile.

Reflectors beneath the Cenozoic section are present in a number of areas beneath California Wash (Figure 7a). At the southern end of LV-3 (Figure 7, kilometers -49 to -46), reflectors form a ~5 km stack that likely represent much of the Paleozoic section in this area (see Page and others, 2005, cross section G-G'). Between kilometers -45 and -40, the reflectors beneath the interpreted base of Cenozoic fill mimic the shape of the strong, overlying reflectors but with steeper dips, a signature consistent with their origin as multiples of the Cenozoic reflector package. Further to the north, deep reflectors are sporadic and weaker, and their origin as primary reflectors from older units or as multiples is unclear.

Langenheim and others (2001b) concluded that California Wash basin was formed primarily by extension on a west-dipping California Wash Fault Zone at the eastern margin of the basin, several kilometers west of a group of young faults active since the late Tertiary (Figure 1b). Page and others (2006) show that east-dipping normal faults at the western side of California Wash basin form the eastern range front of the Arrow Canyon Range. Although these faults do not have sufficient displacement to create significant relief of the basin floor, Page and others (2006) recognized them as part of the east Arrow Canyon Range fault zone, a feature that partly controls ground-water discharge in the Muddy River Springs area. California Wash basin and the neighboring Dry Lake and Arrow Canyon Ranges to the west are underlain by thick Paleozoic carbonate sequences that have been repeated by thrust displacement along the Dry Lake and Muddy Mountain Thrust Faults (Page and others, 2006). This duplex geometry forms the greatest thickness of carbonate aquifer units in the southern Colorado groundwater flow system (Page and others, 2005, 2006).

Implications for Groundwater Studies

Gravity and seismic observations of Tule Desert and Meadow Valley Wash basins indicate the presence of buried basement structures that segment the alluvial sections into subbasins. These features, which are not clear from land topography or geologic mapping, may be important to the groundwater system. For example, they may act as barriers to groundwater flow within the alluvial aquifer along a valley, such that groundwater pumped from the alluvium in one part of a valley might not change water levels in other parts of the valley. Alternatively, basement highs may serve as areas of enhanced groundwater exchange between the alluvial and underlying carbonate aquifer systems, especially if these structures are associated with fractures and faults. While the importance of these intrabasin structures to the groundwater systems of these basins cannot be established without hydrologic testing, their identification with geophysical methods shows where more detailed study is needed.

Most of the basins in the study area are asymmetric in cross section with greater-offset range bounding faults on one side of the basin than on the other (Page and others, 2006). This half-graben asymmetry is reflected in the shape of gravity anomalies and estimated basement depths (Figure 1e). The largest mapped faults and the greatest gravity gradients in Tule Desert are along the eastern margin where the East Tule Desert fault is the dominant fault (Figures 1b and 3). In northern Meadow Valley Wash, the dominant fault zone appears to be the Meadow Valley Wash fault zone along the eastern margin of that portion of the basin (Page and others, 2006). In central Meadow Valley Wash, between Galt and Rox, the center of the negative gravity anomaly and basin thickness maximum (Figure 1e) is located towards the western side of the valley suggesting a change in half-graben vergence. In southern Meadow Valley Wash, south of Rox, the gravity anomaly minimum is again to the east of the axis of the valley. California Wash basin appears to be controlled by a west-dipping normal fault along its eastern margin, as observed in gravity analysis (Figure 1e) and seismic reflection line LV-1 (Langenheim and others, 2001b). This structural configuration of Meadow Valley Wash and California Wash basins is reminiscent, but not identical, to that proposed by Carpenter and Carpenter (1994) based on their analysis of proprietary seismic reflection data and gravity data. The changing vergence of extensional structures along Meadow Valley Wash and California Wash basins may be associated with intervening accommodation zones. Such structures could be important for groundwater exchange from basin to basin.

Acknowledgments

We thank the National Park Service, Water Resources Division for project funding of the regional study, and we thank the Virgin Valley Water District for funding the Tule Desert fieldwork. We are grateful to Ryan Wooley, Frank Chaung, and Bruce Chuchel for conducting the fieldwork. We thank V.E. Langenheim, D.S. Sweetkind, and R.E. Anderson for careful reviews of a draft of this report.

Table 1. Cenozoic basin-fill density-depth functions.

[Density contrasts are basin fill density minus surrounding basement density]

From Jachens & Moring (1990)			From Langenheim and others (2001b)		
Depth range (km)	Sedimentary density contrast (g/cm^3)	Volcanic density contrast (g/cm^3)	Depth range (km)	Sedimentary density contrast (g/cm^3)	[1]Volcanic density contrast (g/cm^3)
0-0.2	-0.65	-0.45	0-0.6	-0.57	-0.40
0.2-0.6	-0.55	-0.40	0.6-1.2	-0.31	-0.35
0.6-1.2	-0.35	-0.35	1.2-1.8	-0.19	-0.25
>1.2	-0.25	-0.25	>1.8	-0.09	-0.25

[1] Langenheim and others (2001b) do not provide a density depth function for the volcanic section, so we adapt that of Jachens and Moring (1990) for the appropriate depth ranges.

Table 2. Physical properties of rock samples grouped by lithology.

[Values for density are averages (±1 standard deviation); values for susceptibility are averages. Mz, Mesozoic; Pz, Paleozoic]

Rock type	Age	Number of samples	Grain density (g/cm^3)	Saturated bulk density (g/cm^3)	Dry bulk density (g/cm^3)	Susceptibility (10^{-3} SI)
Carbonate	Mz & Pz	70	2.66 (0.13)	2.62 (0.16)	2.58 (0.20)	0.01
Clastic sedimentary	Mz & Pz	28	2.54 (0.09)	2.42 (0.14)	2.33 (0.18)	1.2
Metamorphic	Proterozoic	60	2.77 (0.13)	2.75 (0.13)	2.74 (0.14)	7.4
Felsic volcanic	Tertiary	9	2.44 (0.16)	2.29 (0.21)	2.17 (0.27)	0.57
Felsic intrusive	Tertiary	25	2.70 (0.07)	2.66 (0.09)	2.64 (0.10)	12
Intermed.-Mafic volcanic	Tertiary	14	2.86 (0.15)	2.80 (0.18)	2.77 (0.20)	5.4
Intermed.-Mafic intrusive	Tertiary	10	2.86 (0.16)	2.84 (0.16)	2.83 (0.16)	5.1

Literature Cited

Anders, M.H., Christie-Blick, N., and Walker, C.D., 2006, Distinguishing between rooted and rootless detachments - a case study from the Mormon Mountains of Southeastern Nevada: Journal of Geology, v. 114, p. 645-664.

Anderson, R.E., and Barnhard, T.P, 1993, Aspects of three-dimensional strain at the margin of the extensional orogen, Virgin River depression area, Nevada, Utah and Arizona: Geological Society of America Bulletin, v. 105, p. 1019-1052.

Axen, G.J., Wernicke, B.P., Skelly, M.F., and Taylor, W.J., 1990, Mesozoic and Cenozoic tectonics of the Sevier thrust belt in the Virgin River Valley area, southern Nevada, *in* Wernicke, B.P., ed., Basin and Range extensional tectonics near the latitude of Las Vegas, Nevada: Geological Society of America Memoir 176, p. 123-154.

Blakely, R.J., 1996, Potential theory in gravity and magnetic applications: Cambridge University Press, 441 p.

Blakely, R.J., and Simpson, R.W., 1986, Approximating edges of source bodies from magnetic or gravity anomalies: Geophysics, v. 51, p. 1494-1498.

Bohannon, R.G., Grow, J.A., Miller, J.J., and Blank, R.H., Jr., 1993, Seismic stratigraphy and tectonic development of Virgin River depression and associated basins, southeastern Nevada and northwestern Arizona: Geological Society of America Bulletin, v. 105, p. 501-520.

Bunch, R.L, and J.R. Harrill, 1984, Compilation of selected hydrologic data from the MX missile-siting investigation, east-central Nevada and western Utah: U.S. Geological Survey Open-File Report 84-702, 123 p.

Carpenter, J.A., and Carpenter, D.G., 1994, Analysis of basin-range and fold-thrust structure, and reinterpretation of the Mormon Peak Detachment and similar features as gravity slide systems; Southern Nevada, Southwest Utah, and Northwest Arizona, *in* Dobbs, S.W., and Taylor, W.J., eds.: Nevada Petroleum Society 1994 Conference Volume II, (Book 1), p. 15-52.

Duebendorfer, E.M., and Black, R.A., 1992, Kinematic role of transverse structures in continental extension: an example from the Las Vegas Valley shear zone, Nevada: Geology, v. 20, p. 1107-1110.

Duebendorfer, E.M., and Simpson, D.A., 1994, Kinematics and timing of Tertiary extension in the western Lake Mead region, Nevada: Geological Society of America Bulletin, v. 106, p. 1057-1073.

Eakin, T.E., and Winograd, I.J., 1965, Interbasin movement of ground water in south central Nevada-Some implications: Geological Society of America Special Paper 82, 52p.

Eaton, G.P., Wahl, R.R., Prostka, H.J., Mabey, D.R., Kleinkopf, M.D., 1978, Regional gravity and tectonic patterns – Their relation to late Cenozoic epeirogeny and lateral spreading of the western Cordillera: Geological Society of America Memoir 152, p. 51-91.

Garside, L.J., Hess, R.H., Fleming, K.L., and Weimer, B.S., 1988, Oil and Gas development in Nevada: Nevada Bureau of Mines and Geology Bulletin 104, 136 p.

Glancy, P.A., and Van Denburgh, A.S., 1969, Water-resources appraisal of the lower Virgin River Valley area, Nevada, Arizona, and Utah: Nevada Department of Conservation and Natural Resources Water Resources-Reconnaissance Series Report 51, 87 p.

Harrill, J.R., Gates, J.S., and Thomas, J.M., 1988, Major ground-water flow systems in the Great Basin region of Nevada, Utah, and adjacent stats: U.S. Geological Survey Hydrologic Investigations Atlas HA-694-C, scale 1:1,000,000.

Harrill, J.R., and Prudic, D.E., 1998, Aquifer systems in the Great Basin region of Nevada, Utah and adjacent states—Summary report: U.S. Geological Survey Professional Paper 1409A, 61 p.

Healey, D.L, Clutsom, F.G., and Glover, D.A., 1984, Borehole gravity meter surveys in drill holes USW G-3, UE-25p1, and UE-25c1: U.S. Geological Survey Open-File Report 84-672, 16 p.

Hess, R.H., 2004, Nevada oil and gas well database (NVOILWEL), Nevada Bureau of Mines and Geology Open-File Report 04-1, 288 p.

Hintze, L.F., and Axen, G.J., 2001, Geologic map of the Lime Mountain Quadrangle, Lincoln County, Nevada: Nevada Bureau of Mines and Geology Map 129, scale 1:24,000.

HydroSystems, Inc., 2002, Tule Desert field activity and data report: Tempe, Ariz., 16 p.

Jachens, R.C., and Moring, B.C., 1990, Maps of the thickness of Cenozoic deposits and the isostatic residual gravity over basement for Nevada: U.S. Geological Survey Open-File Report 90-404, 15 p., 2 plates, scale 1:1,000,000.

Jachens, R.C., Dixon, G.L., Langenheim, V.E., and Morin, R., 1998, Interpretation of an aeromagnetic survey over part of Virgin Valley, Tule Desert, and the valley surrounding Meadow Valley Wash, southeastern Nevada: U.S. Geological Survey Open-File Report 98-804, 16 p.

Johnson, G.R., and Olhoeft, G.R., 1984, Density of rocks and minerals, *in* Carmichael, R.S., ed., CRC Handbook of Physical Properties of Rocks, Vol. 3: Boca Raton, Fla., CRC Press, Inc., p. 1-38.

Kane, M.F., Healey, D.L, Peterson, D.L., Kaufmann, H.E., and Reidy, D., 1979, Bouguer gravity map of Nevada – Las Vegas sheet: Nevada Bureau of Mines and Geology Map 61, scale 1:250,000.

Langenheim, V.E., Davidson, J.G., Anderson, M.L., and Blank, H.R., Jr., 1999, Geophysical constraints on the Virgin River depression, Nevada, Utah, and Arizona: U.S. Geological Survey Open-File Report 99-435, 26 p.

Langenheim, V.E., Glen, J.M., Jachens, R.C., Dixon, G.L., Katzer, T.C., and Morin, R.L., 2000, Geophysical constraints on the Virgin River depression, Nevada, Utah, and Arizona: U.S. Geological Survey Open-File Report 00-407, 26 p.

Langenheim, V.E., Bohannon, R.G., Glen, J.M., Jachens, R.C., Grow, J.A., Miller, J.J., Dixon, G.L., and Katzer, T.C., 2001a, Basin configuration of the Virgin River depression, Nevada, Utah, and Arizona-A geophysical view of deformation along the Colorado Plateau-Basin and Range transition, in Erskine, M.C., Faults, J.E., Bartley, J.M., and Rowley, P.D., eds., The geologic transition, High Plateaus to Great Basin-A symposium and field guide (The Mackin Volume): Utah Geological Association and Pacific Section of the American Association of Petroleum Geologists: Utah Geological Association Publication 30, p. 205-226.

Langenheim, V.E., Miller, J.J., Page, W.R., and Grow, J.A., 2001b, Thickness and geometry of Cenozoic deposits in California Wash area, Nevada, based on gravity and seismic reflection data: U.S. Geological Survey Open-File Report 01-393, 24 p.

Morelli, C., 1974, The International Gravity Standardization Net 1971: International Association of Geodesy Special Publication no. 4, 194 p.

Page, W.R., Dixon, G.L., Rowley, P.D, and Brickey, D.W., 2005, Geologic map of parts of the Colorado, White River, and Death Valley groundwater flow systems, Nevada, Utah, and Arizona: Nevada Bureau of Mines and Geology Map 150, 1:250,000-scale.

Page, W.R., Scheirer, D.S., Langenheim, V.E., 2006, Geologic cross sections of parts of the Colorado, White River, and Death Valley regional ground-water flow systems, Nevada, Utah, and Arizona: U.S. Geological Survey Open-File Report 2006-1040, 23 p.

Phelps, G.A., Jewel, E.B., Langenheim, V.E., and Jachens, R.C., 2000, Principal facts for gravity stations in the vicinity of Coyote Spring Valley, Nevada, with initial gravity modeling results: U.S. Geological Survey Open-File Report 00-420, 18 p.

Plouff, D., 1977, Preliminary documentation for a FORTRAN program to compute gravity terrain corrections based on topography digitized on a geographic grid: U.S. Geological Survey Open-File Report 77-535, 45 p.

Ponce, D.A., 1997, Gravity data of Nevada: U.S. Geological Survey Digital Data Series DDS-42, 27 p, CD-ROM.

Quigley, M.C., Karlstrom, K., Beard, S., and Bohannon, R.G., 2002, Influence of Proterozoic and Laramide structures on the Miocene extensional strain field, north Virgin Mountains, Nevada/Arizona, *in* Lund, W.R., ed., Field Guide to Geologic Excursions in Southwestern Utah and Adjacent areas of Arizona and Nevada, Geological Society of America Rocky Mountain Section Meeting, Cedar City, Utah, May 7th-9th, 2002; U.S. Geological Survey Open-File Report 02-172, p. 86-104.

Rowley, P.D., Nealey, L.D., Unruh, D.M., Snee, L.W., Mehnert, H.H., Anderson, R.E., and Gromme, C.S., 1995, Stratigraphy of Miocene ash-flow tuffs in and near the Caliente Caldera complex, southeastern Nevada and southwestern Utah, in Scott, R.B., and Swadley, W.C., eds., Geologic studies in the Basin and Range-Colorado Plateau transition in southeastern Nevada, southwestern Utah, and northwestern Arizona, 1992: U.S Geological Survey Bulletin 2056, p. 43-88.

Rush, F.E., 1964, Ground-water appraisal of the Meadow Valley area, Lincoln and Clark Counties, Nevada: Nevada Department of Conservation and Natural Resources Water Resources-Reconnaissance Series Report 27, 43 p.

Rush, F.E., 1968, Water-resources appraisal of the Lower Moapa-Lake Mead Area, Clark County, Nevada: Nevada Department of Conservation and Natural Resources Water Resources-Reconnaissance Series Report 50, 66 p.

Saltus, R.W., and Jachens, R.C., 1995, Gravity and basin-depth maps of the Basin and Range Province, western United States: U.S. Geological Survey Geophysical Investigations Map GP-1012, 15 p., scale 1:2,500,000.

Scott, R.B., Gromme, C.S., Best, M.G., Rosenbaum, J.G., and Hudson, M.R., 1995, Stratigraphic relationships of Tertiary volcanic rocks in central Lincoln County, southeastern Nevada, in Scott, R.B., and Swadley, W.C., eds., Geologic studies in the Basin and Range-Colorado Plateau transition in southeastern Nevada, southwestern Utah, and northwestern Arizona, 1992: U.S Geological Survey Bulletin 2056, p. 5-42.

Simpson, R.W., Jachens, R.C., Blakely, R.J., and Saltus, R.W., 1986, A new isostatic residual gravity map of the conterminous United States with a discussion on the significance of isostatic residual anomalies: Journal of Geophysical Research, v. 91, p. 8348-8372.

Snyder, D.B., Wahl, R.R., and Currey, F.E., 1981, Bouguer gravity map of Nevada – Caliente sheet: Nevada Bureau of Mines and Geology Map 70, scale 1:250,000.

Stewart, J.H., and Poole, F.G., 1972, Lower Paleozoic and uppermost Precambrian Cordilleran Miogeocline, Great Basin, western United States, *in* Dickinson, W.R., ed., Tectonics and Sedimentation, Society of Economic Paleontologists and Mineralogists Special Publication 22, p. 28-57.

Syberg, F.R.J., 1972, A Fourier method for the regional-residual problem of potential fields: Geophysical Prospecting, v. 20, 47-75.

Talwani, M., Worzek, J.L, and Landisman, M., 1959, Rapid gravity computations for two-dimensional bodies with application to the Mendocino submarine fracture zone: Journal of Geophysical Research, v. 64, p. 49-59.

Wernicke, Brian, Walker, D.J., and Beaufait, M.S., 1985, Structural discordance between Neogene detachments and frontal Sevier thrusts, Central Mormon Mountains, Southern Nevada: Tectonics, v. 4, no. 2, p. 213-246.

Zonge Engineering and Research Organization, Inc., 2002, Geophysical data in the Tule Desert, Lincoln County, Nevada: Tucson, Ariz., 17 p.

Appendix: Seismic Imaging Quality

The quality of seismic imaging beneath the valleys of the study area varies considerably from basin to basin, and there is a general correlation between image quality and surface geology and morphology. The best seismic image of basin-fill material occurs in California Wash (Figure 7) where the land topography is smooth (Figure 1a) and where Quaternary, fine-grained sedimentary deposits are at the surface (Figure 1b). In Meadow Valley Wash basin, the section of LV-3 from Moapa to Rox (Figure 5) images the basin-fill better than does the portion north of Rox (Figures 5 and 4); the former section corresponds to a region of Quaternary deposition and the latter section corresponds to an environment where Tertiary units are being eroded (Figure 1b). The roughness of the land topography along LV-3 increases moving northward through Meadow Valley Wash (Figure 1a). We suggest three explanations for this variation in imaging quality: first, that finer-grained and younger deposits present a higher-fidelity near-surface medium for the passage of seismic source and received reflection energy than do coarser-grained sediments; second, that the interaction of seismic energy with rougher land-topography introduces higher levels of noise in the seismic recordings; and third, that the older basin fill deposits are likely to have experienced greater deformation than their younger counterparts, which would lead to less continuous and more-steeply dipping deposits that are more poorly suited to seismic reflection imaging. The relative importance of these explanations cannot be established with the current seismic reflection data set.

While the seismic reflection lines predominantly cross Quaternary and Tertiary sedimentary deposits, there are two small sections where they cross other units: LV-3 north of Galt crosses Paleozoic carbonate units (Figure 4, kilometers 30-38), and LV-6 between Meadow Valley Wash and Tule Desert basins crosses Tertiary volcanic rocks (Figure 3, kilometers 6-8). In both of these sections, no coherent reflectors are observed. In the case of LV-3 north of Galt, the ~30° westward dip of the lower Permian-upper Mississippian units may present imaging difficulties for the north-south-oriented LV-3 line. As a single line, LV-3 was processed via stacking and migration analysis to enhance structures that strike perpendicular to the seismic profile. In the case of LV-6 crossing the volcanic ridge between the Clover and Mormon Mountains, the lack of reflectivity suggests that the volcanic units do not contain significant, subhorizontal interfaces with physical property contrasts. While the eastward extent of the Tertiary volcanic units buried beneath Tule Desert is not known (in our gravity forward model, we suggest that they end near the buried ridge, Figure 3d), we speculate that the near-surface volcanic units obscure the seismic imaging of underlying Paleozoic units, which are observed as strong reflectors east of the buried ridge (Figure 3). The cause of such obscuring might be related to intrinsic seismic attenuation of the reflection energy within the volcanic units, or it might be caused by greater levels of incoherent scattering of energy that is transmitted through the volcanic unit.

These observations and explanations of seismic image quality in the study basins may be useful in guiding seismic reflection acquisition and interpretation elsewhere in southern Nevada. The best reflection images were obtained where the seismic lines were oriented perpendicular to the main geologic structures (LV-6 and LV-2A, Figures 3 and 6) and where shallow sedimentary deposits have subhorizontal bedding (e.g. LV-3 across California Wash, Figure 7). Seismic imaging degrades where surface topography is rough and where near-surface deposits have been deformed (e.g. the northern sections of LV-3, Figures 4 and 5). Volcanic units at the western end of Tule Desert appear to be without significant stratification of physical properties, and they may obscure reflections from underlying units.

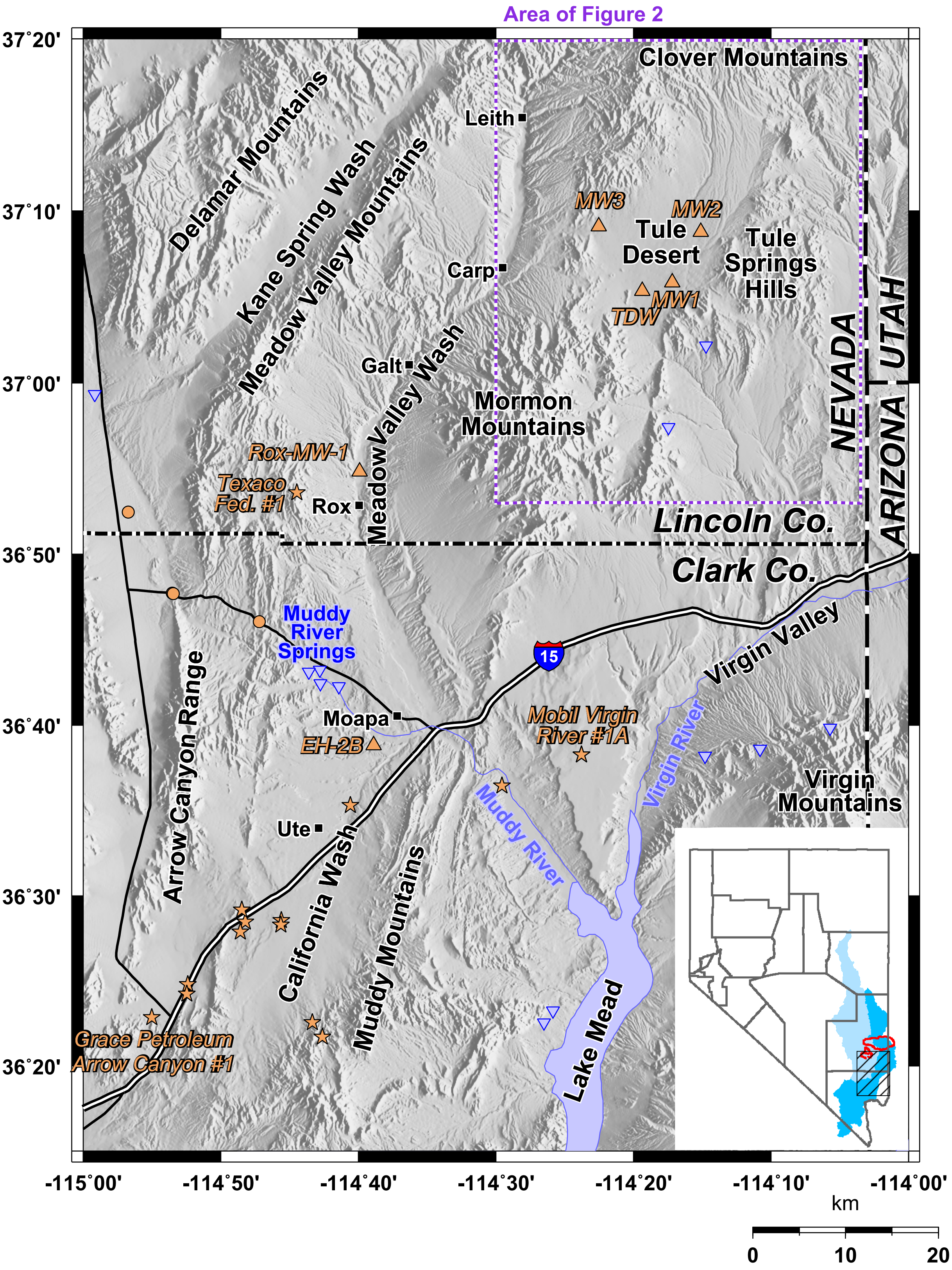

Figure 1. (1a) Shaded-relief map of the study area. Blue triangles denote springs; brown triangles denote water wells used in this report, brown stars indicate oil and gas well locations; brown circles indicate large-diameter MX well locations; purple dotted line denotes area of Figure 2. Inset shows study area (hachured box) within Nevada, along with the White River Regional Groundwater Flow System (light blue) and the remainder of the Lower Colorado Regional Groundwater Flow System (dark blue). In the inset, red lines denote the Caliente caldera complex, immediately to the north of the study area, and the Kane Spring Wash caldera complex in the northernmost portion of the study area.

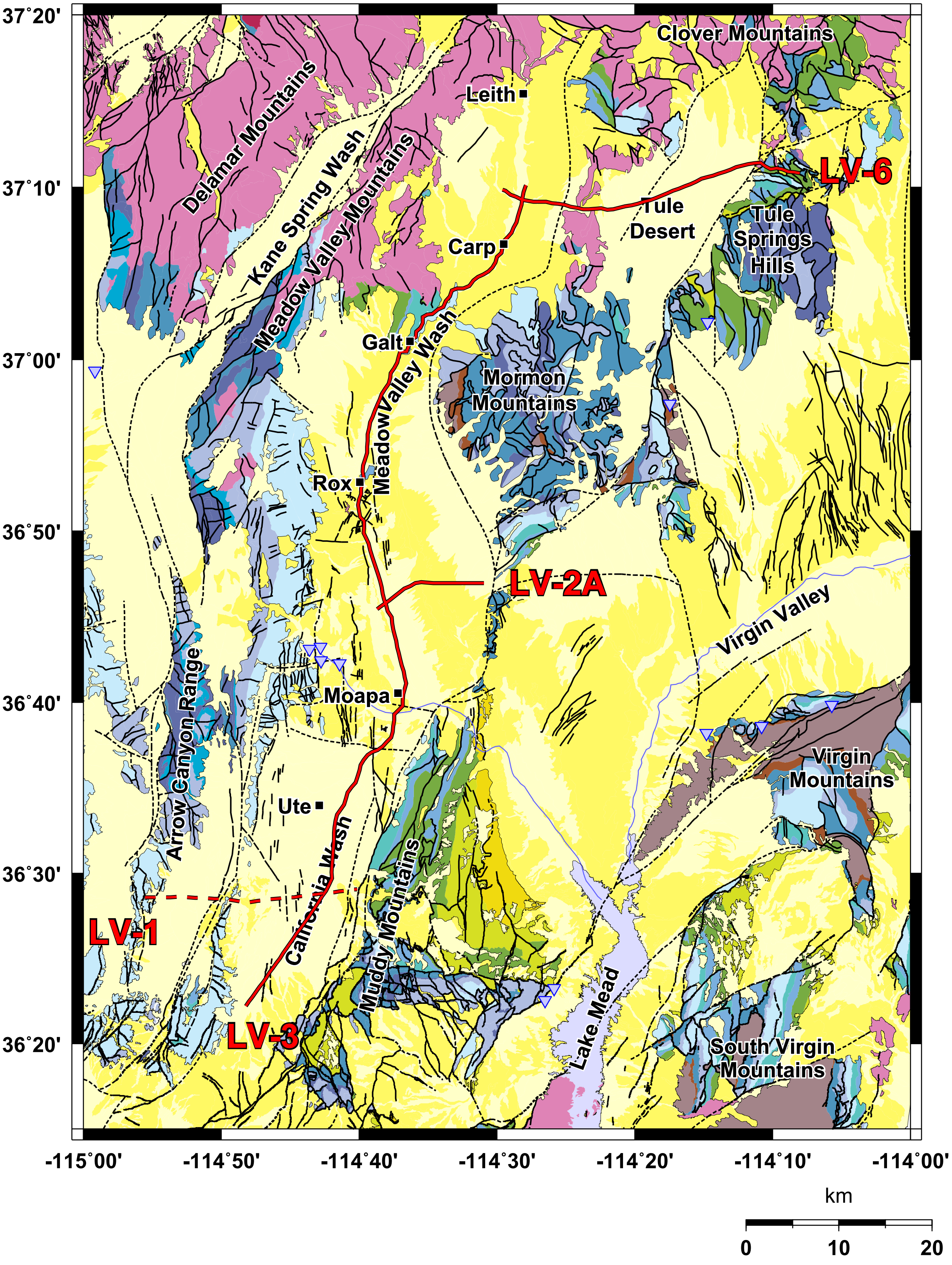

Figure 1 (continued). (1b) Geologic map of the study area modified from Page and others (2005); the grouping of geologic units is based on Page and others (2006). We subdivide the Page and others (2006) QTu sedimentary unit into younger (QTuy, middle Pleistocene and younger) and older (QTuo, early Pleistocene and older) units. Seismic reflection lines are indicated in red.

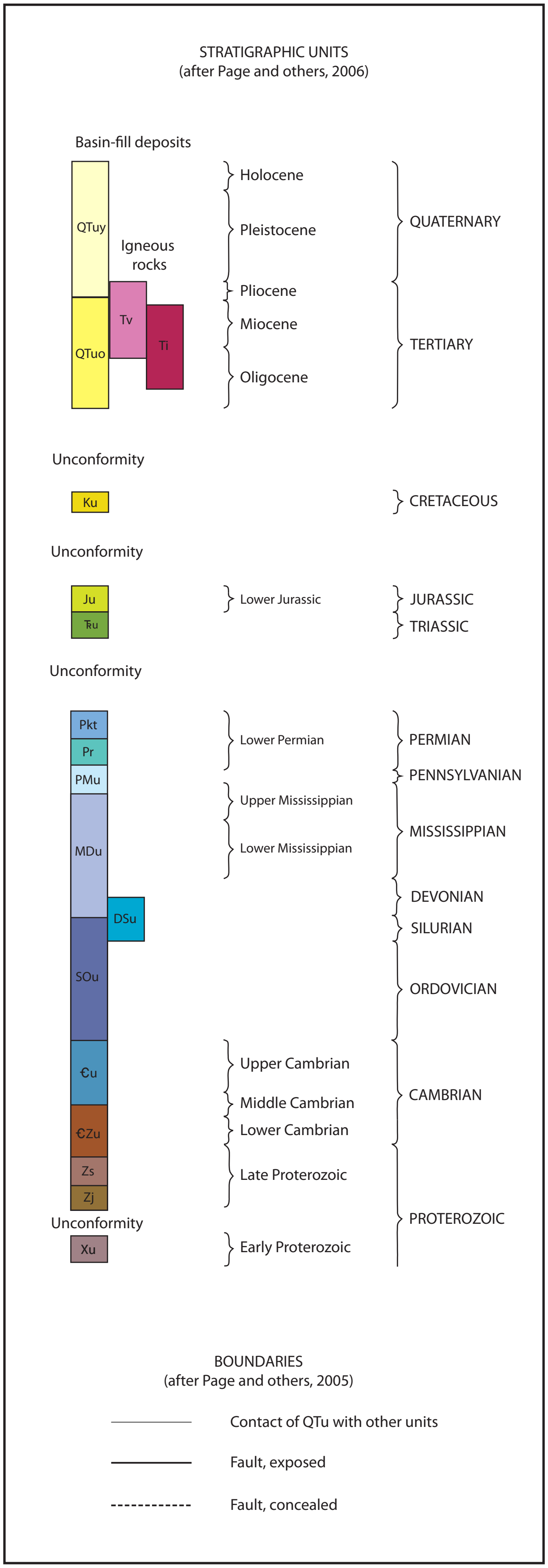

Figure 1 (continued). (1b, continued)

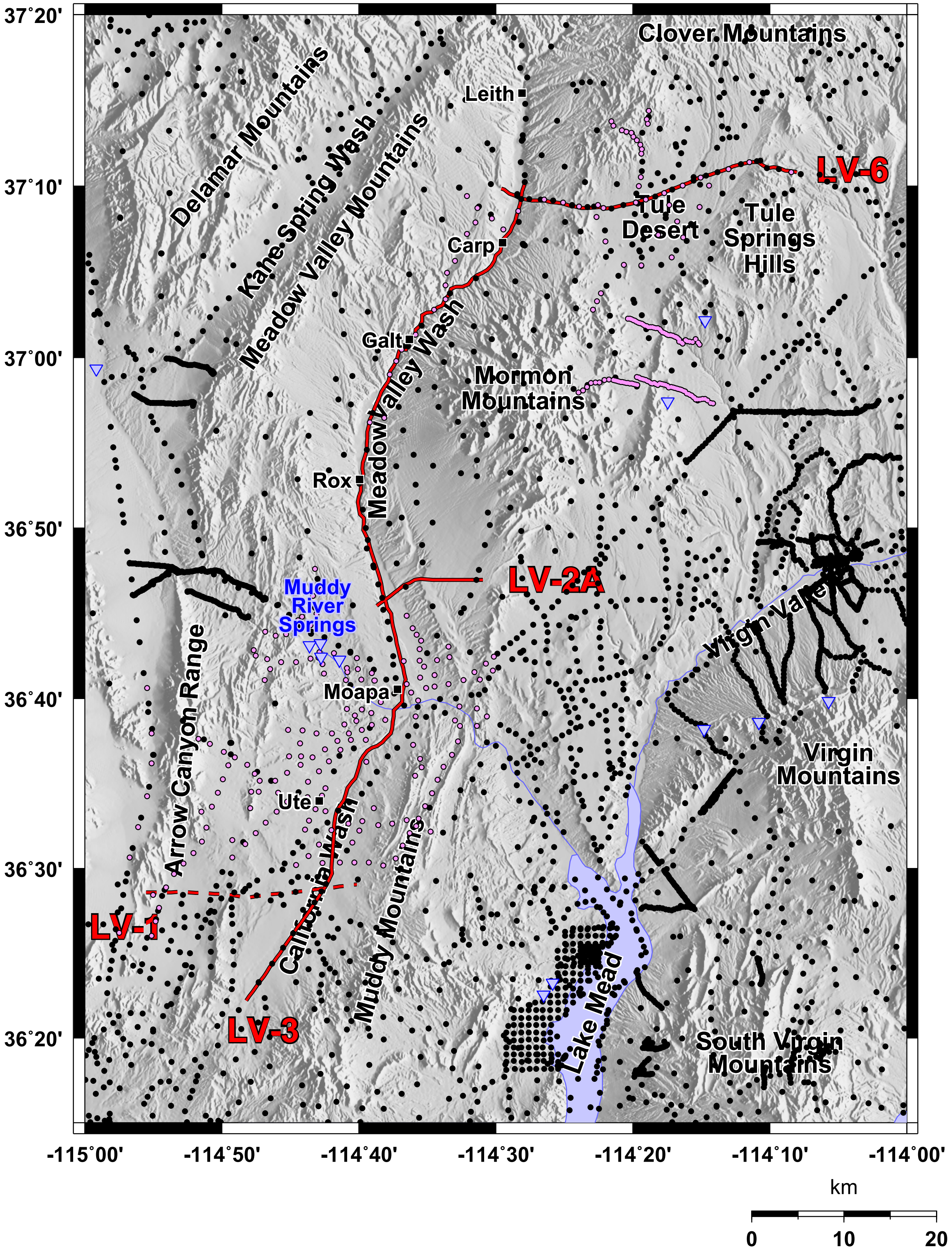

Figure 1 (continued). (1c) Gravity stations of the study area, with stations collected by the USGS in 2002 and 2003 denoted in pink and prior stations denoted in black. Red lines indicate positions of four seismic reflection profiles; the three solid lines are those investigated in this report, and the dashed line (LV-1) was analyzed in Langenheim and others (2001b).

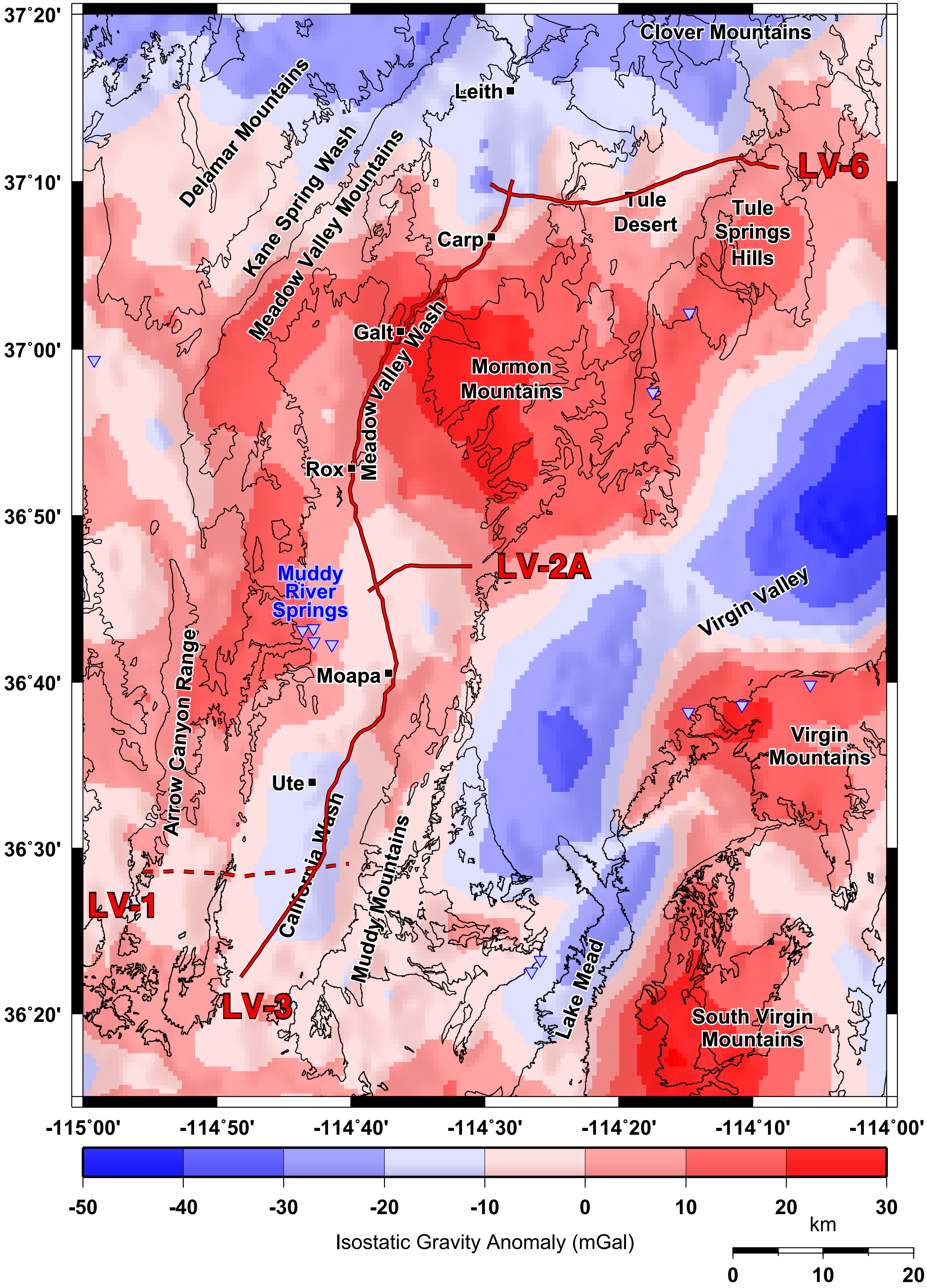

Figure 1 (continued). (1d) Isostatic gravity anomaly map of the study area. Thin lines mark the contacts of QTu with other units, which serve to outline the ranges.

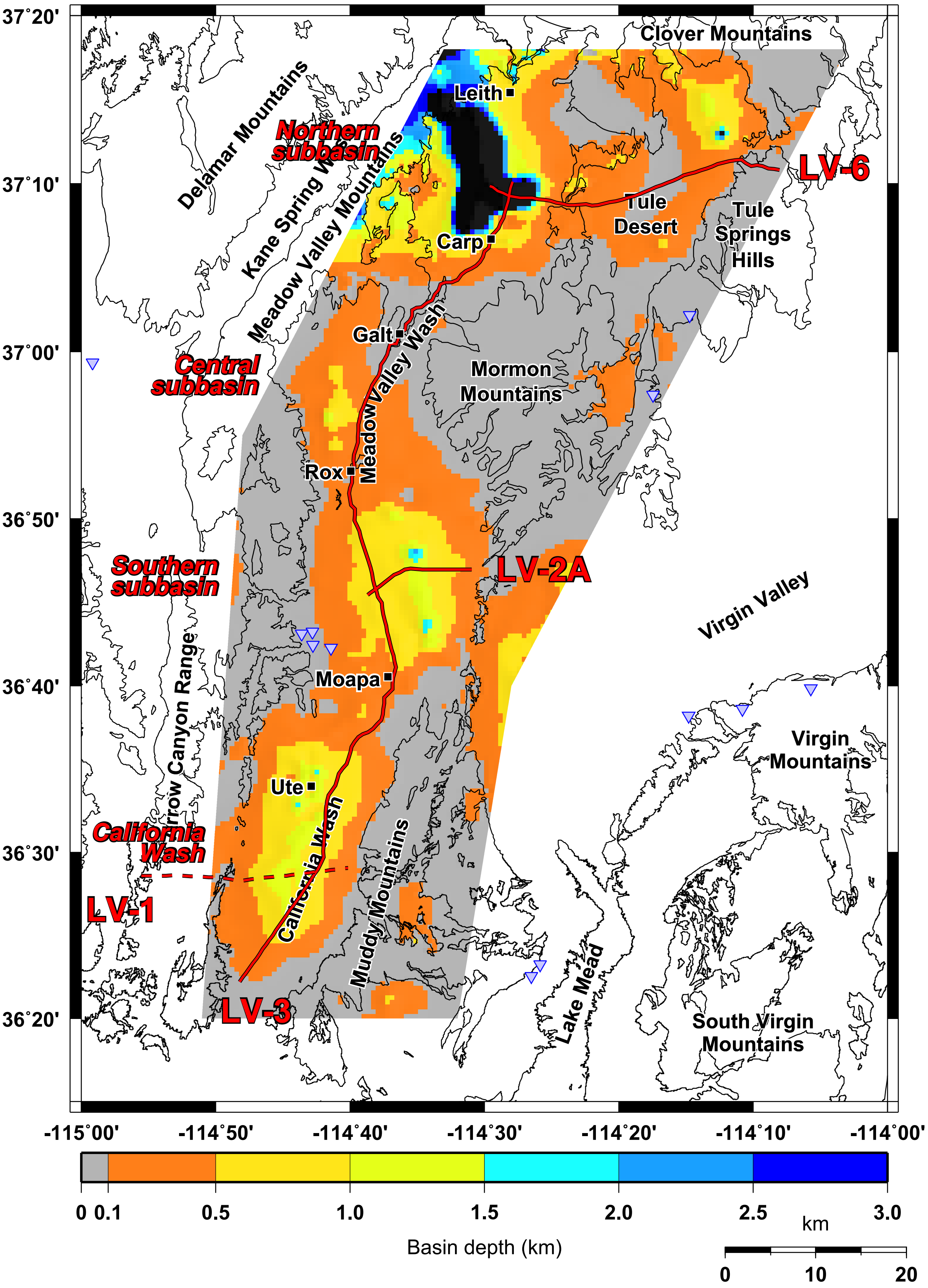

Figure 1 (continued). (1e) Model of depth to basement for Tule Desert, Meadow Valley Wash, and California Wash basins, estimated from gravity analysis.

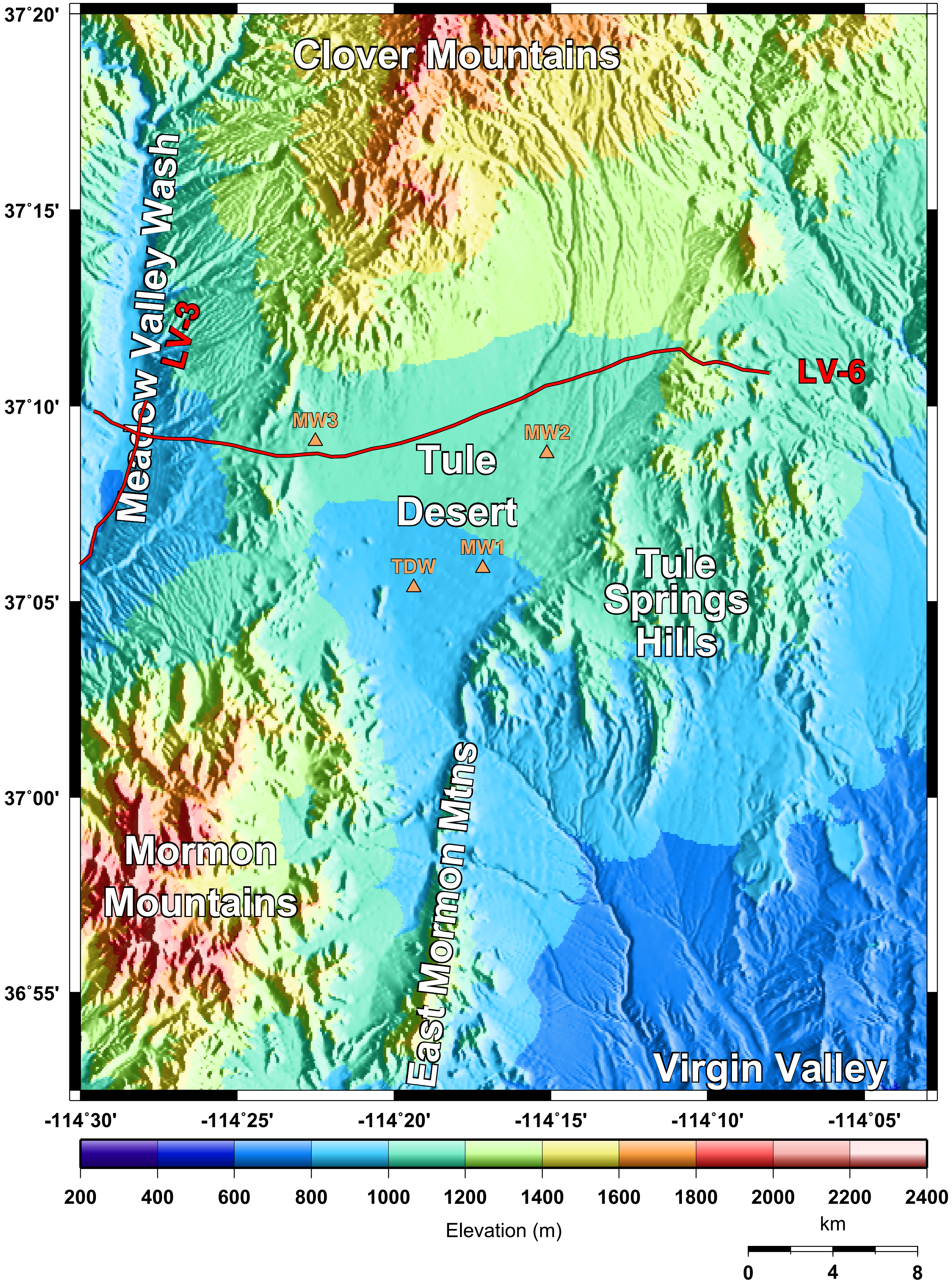

Figure 2. (2a) Topographic map of Tule Desert and adjacent Meadow Valley Wash. Water wells are indicated by brown triangles, and seismic profiles by red lines.

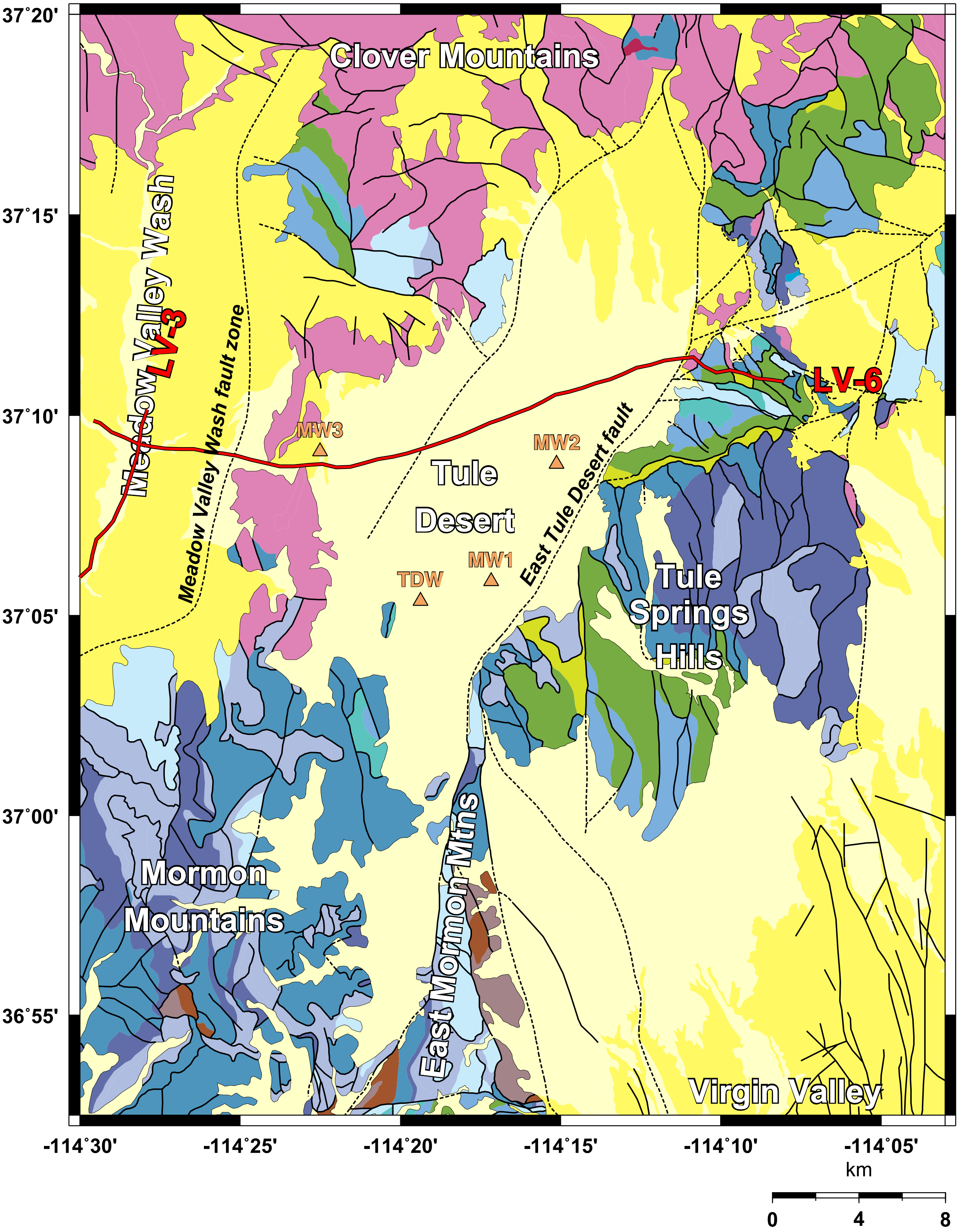

Figure 2 (continued). (2b) Enlargement of geologic map in Figure 1b covering the Tule Desert area; see Figure 1b for explanation of geologic units.

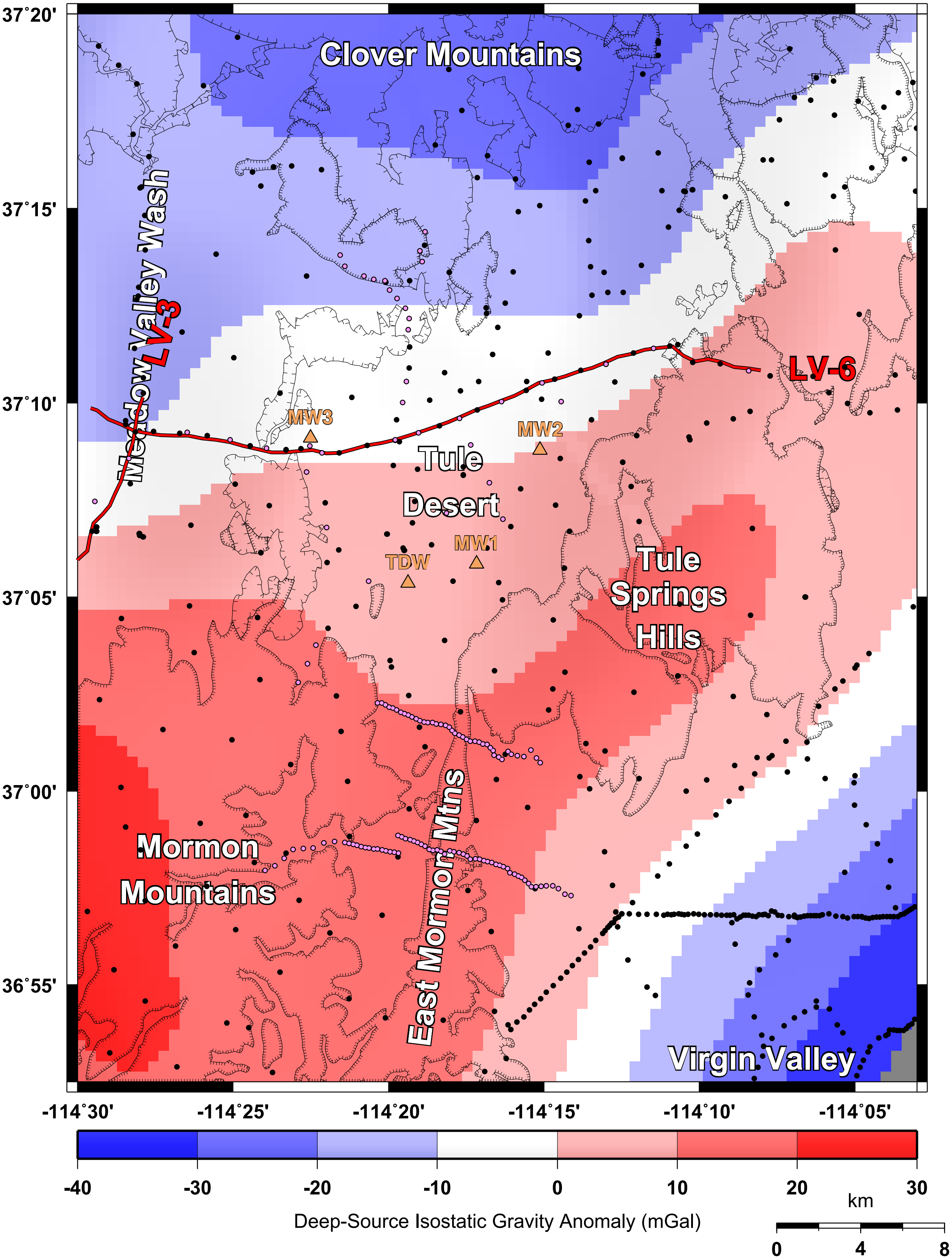

Figure 2 (continued). (2c) Map of the component of the isostatic gravity anomaly that arises from deep sources. Thin solid lines mark the contact of QTu with other units; close-spaced hachures enclose pre-Cenozoic basement units, while wider-spaced hachures enclose Tertiary igneous outcrop. Red lines indicate seismic reflection profiles, and circles denote gravity stations (pink, collected in 2002; black, collected before 2002).

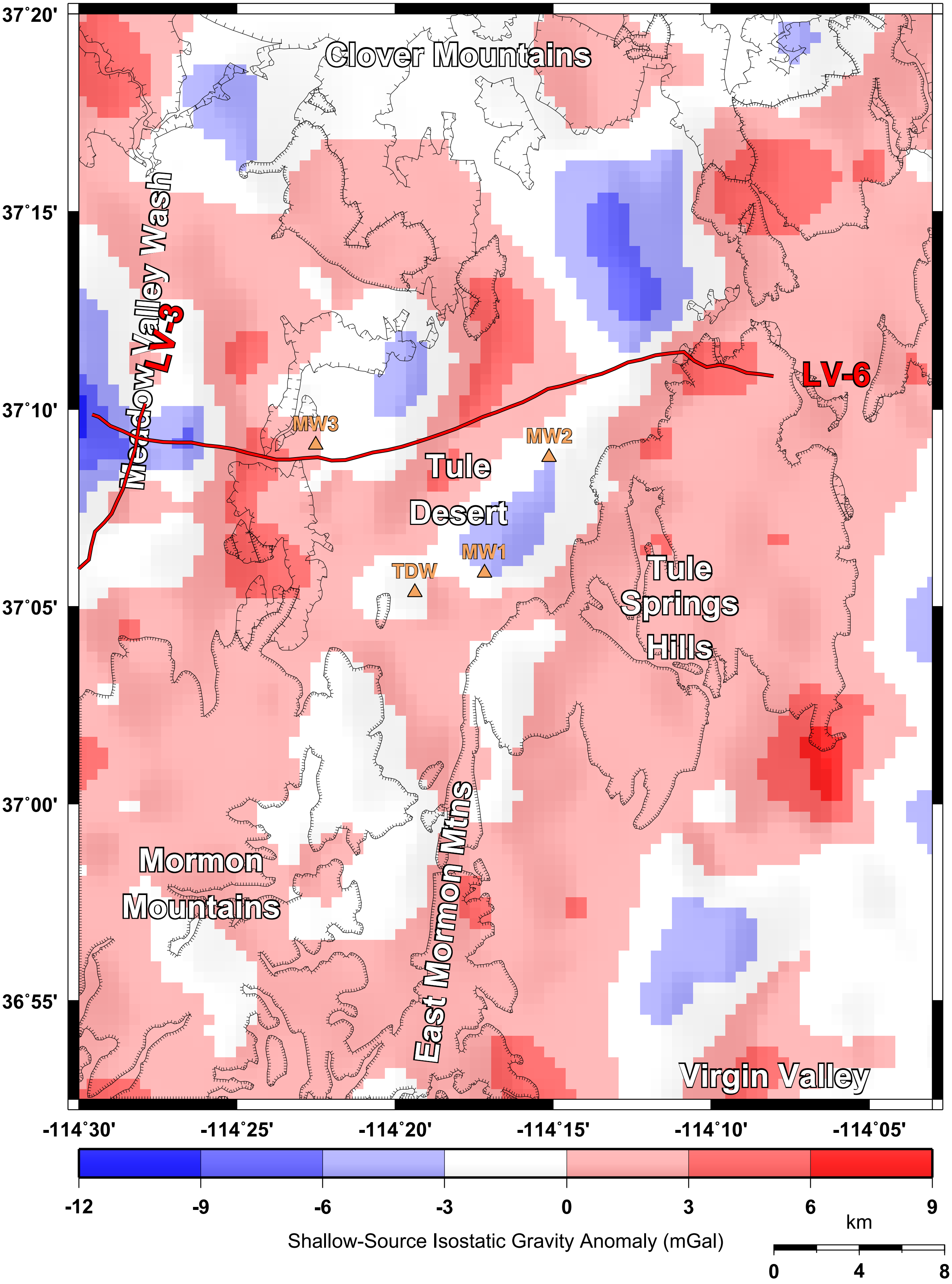

Figure 2 (continued). (2d) Map of the shallow-depth source contribution to the isostatic gravity anomaly with hachured lines as in Figure 2c.

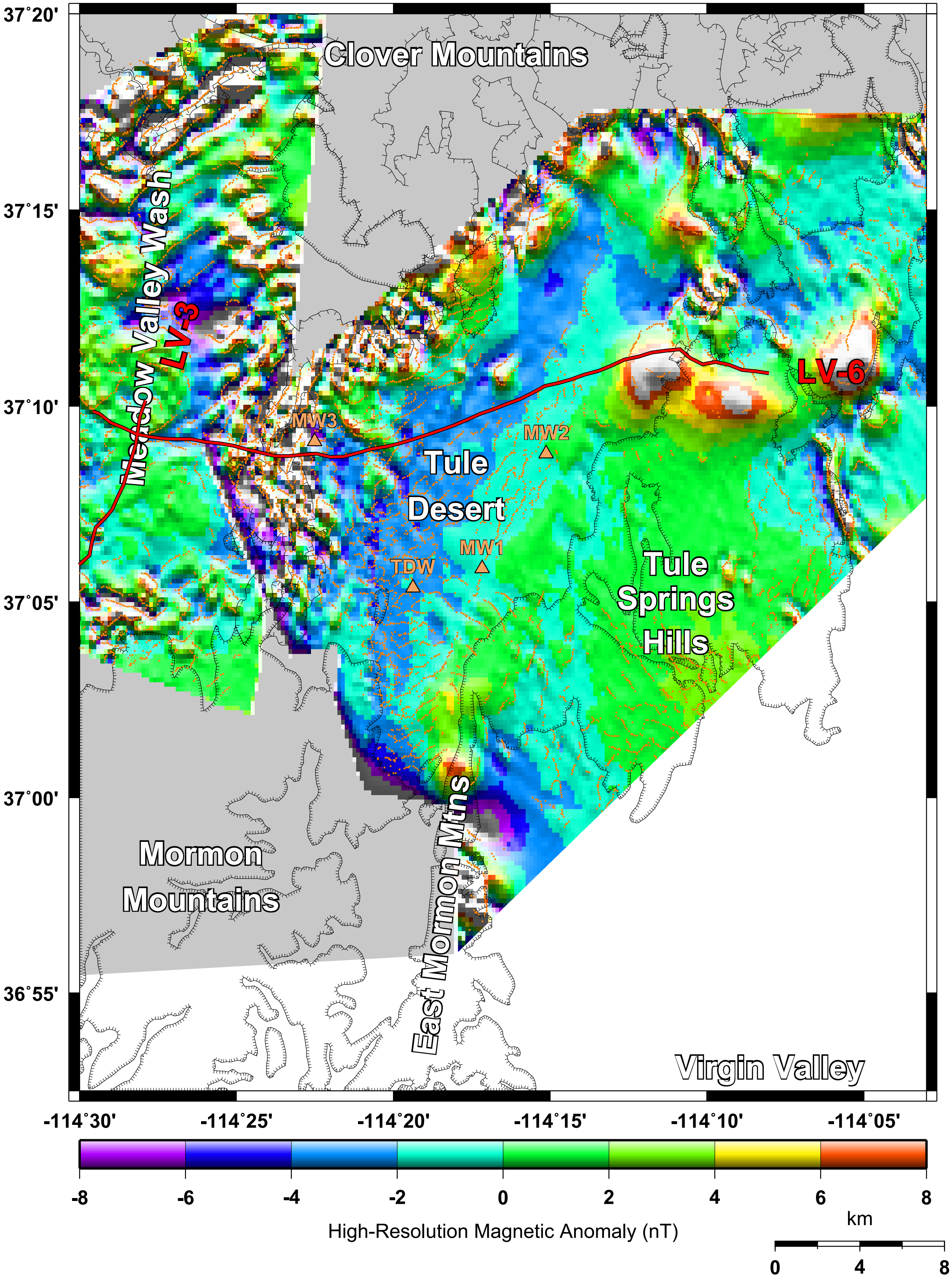

Figure 2 (continued). (2e) High-resolution aeromagnetic map (Jachens and others, 1998) that emphasizes magnetic sources in the shallow subsurface. Orange points indicate the locations of the largest 75% of maximum horizontal gradients of the high-resolution magnetic field, which mark the edges of shallow magnetic bodies.

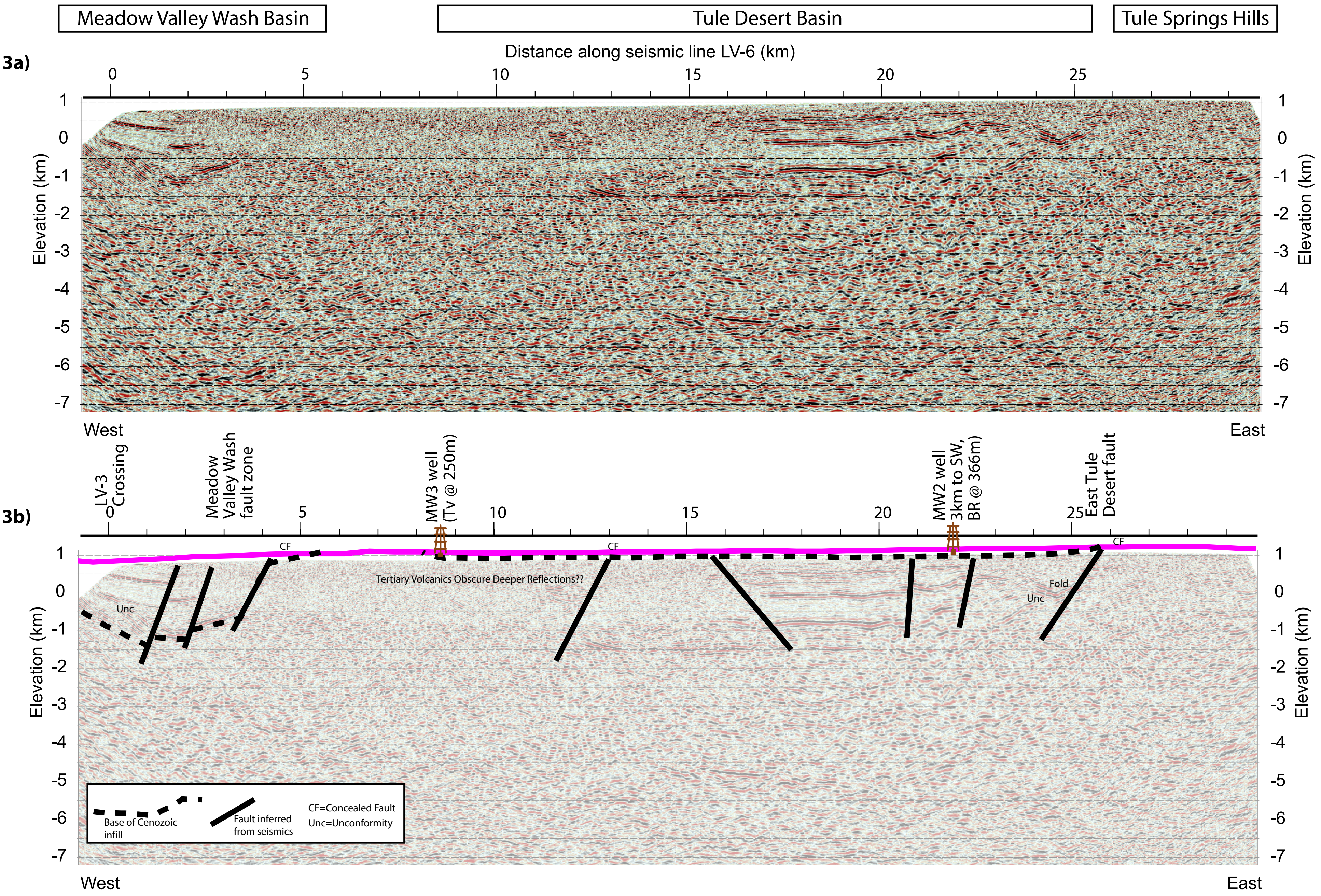

Figure 3. Migrated seismic reflection line LV-6 crossing Meadow Valley Wash and Tule Desert basins, displayed with no vertical exaggeration. (3a) Uninterpreted section. (3b) Interpreted section, with magenta line indicating land surface. Along-line distances in kilometers are east of LV-3 crossing. Tv, Tertiary volcanics; BR @ 366 m, basement intersected drill hole at 366 m depth; Unc., unconformity; CF, concealed fault. The MW2 well symbol is projected to the seismic line along the strike of the East Tule Desert fault.

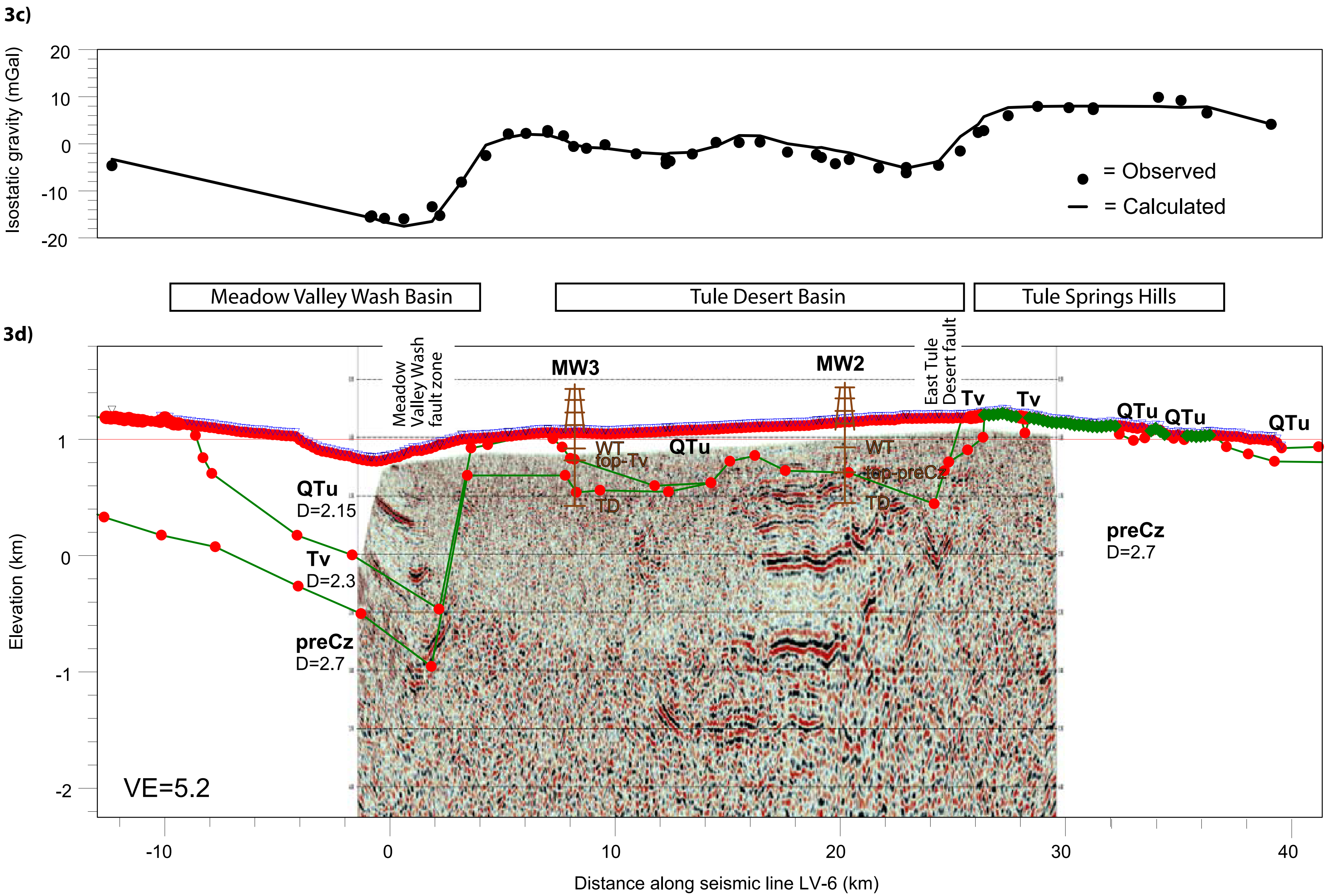

Figure 3 (continued). (3c) Isostatic gravity anomaly and predicted gravity along the seismic line. (3d) Density model superimposed on the seismic reflection profile. The ~5-fold increase in vertical exaggeration provides a different view of the seismic data from that of Figure 3a. The density model extends linearly ~10 km beyond the both ends of the seismic profile. QTu, Quaternary and Tertiary undifferentiated sediment; Tv, Tertiary volcanics; preCz, pre-Cenozoic rocks; WT, water table; TD, total depth of well. The "D=" values are densities in grams/cubic centimeter.

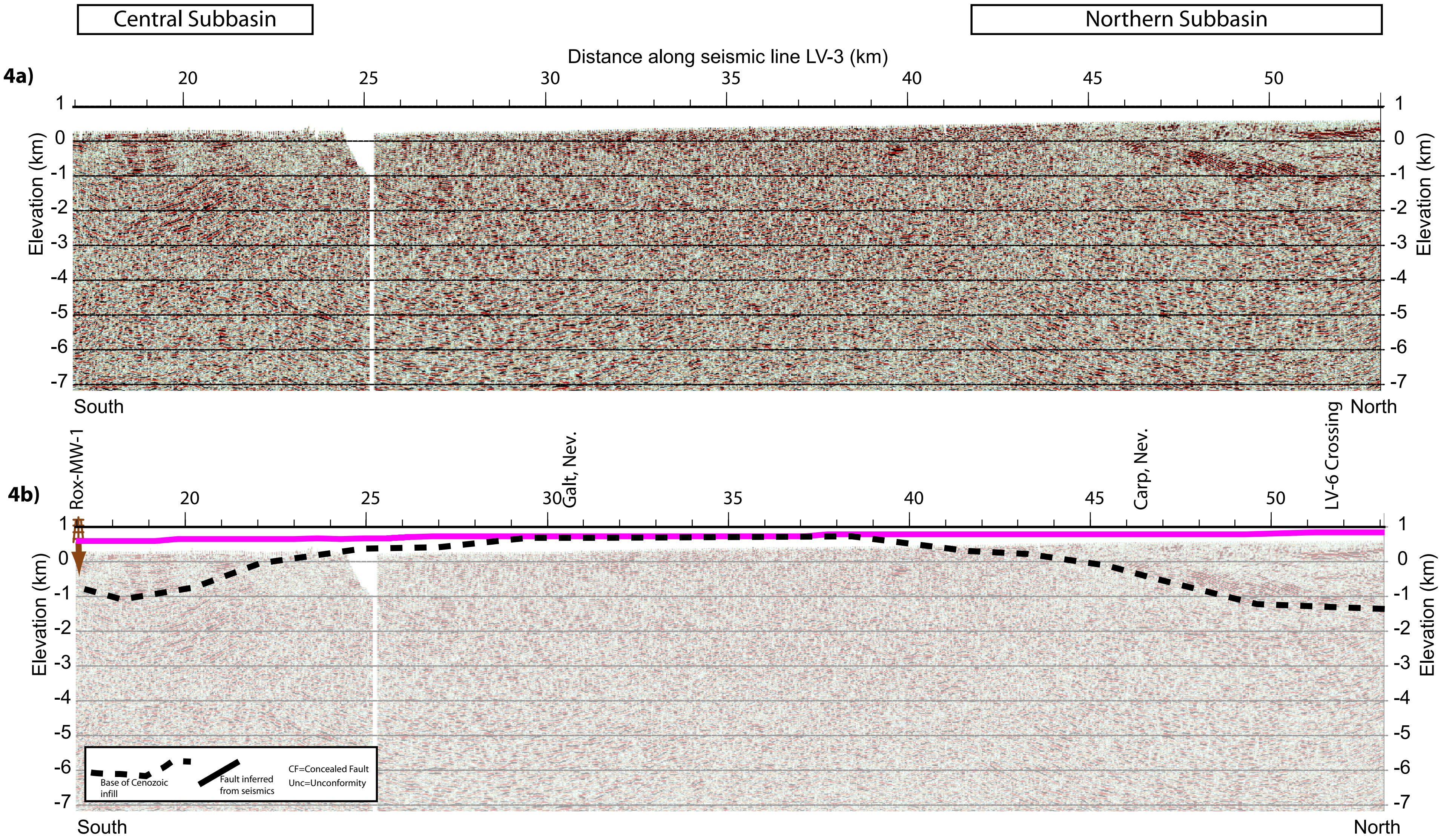

Figure 4. Migrated seismic reflection line LV-3 along northern Meadow Valley Wash basin, displayed with no vertical exaggeration. (4a) Uninterpreted section. (4b) Interpreted section, with magenta line indicating land surface. Along-line distances in kilometers are north of LV-2A crossing.

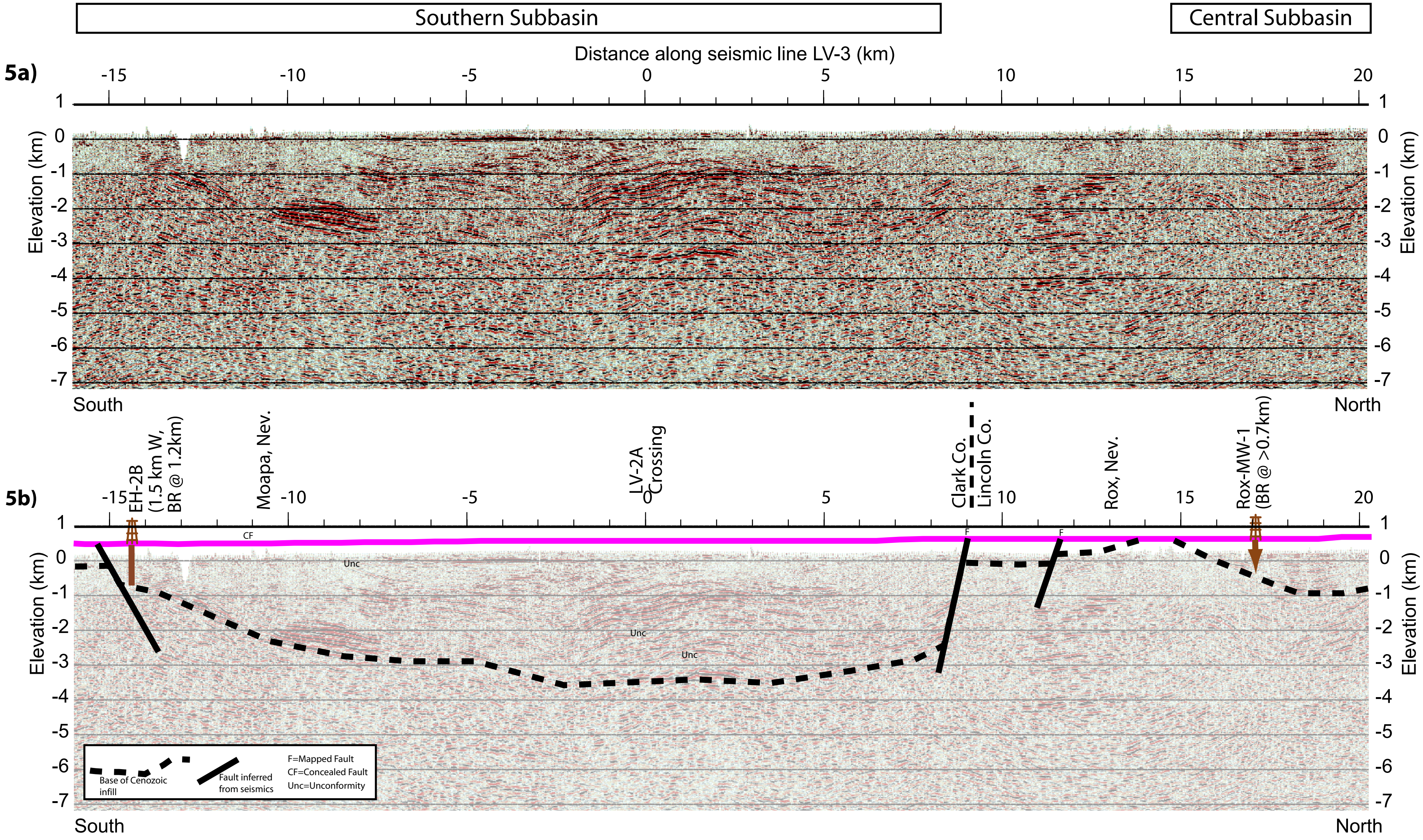

Figure 5. Migrated seismic reflection line LV-3 along southern Meadow Valley Wash basin, displayed with no vertical exaggeration. (5a) Uninterpreted section. (5b) Interpreted section, with magenta line indicating land surface. Along-line distances in kilometers are north of LV-2A crossing. BR, basement.

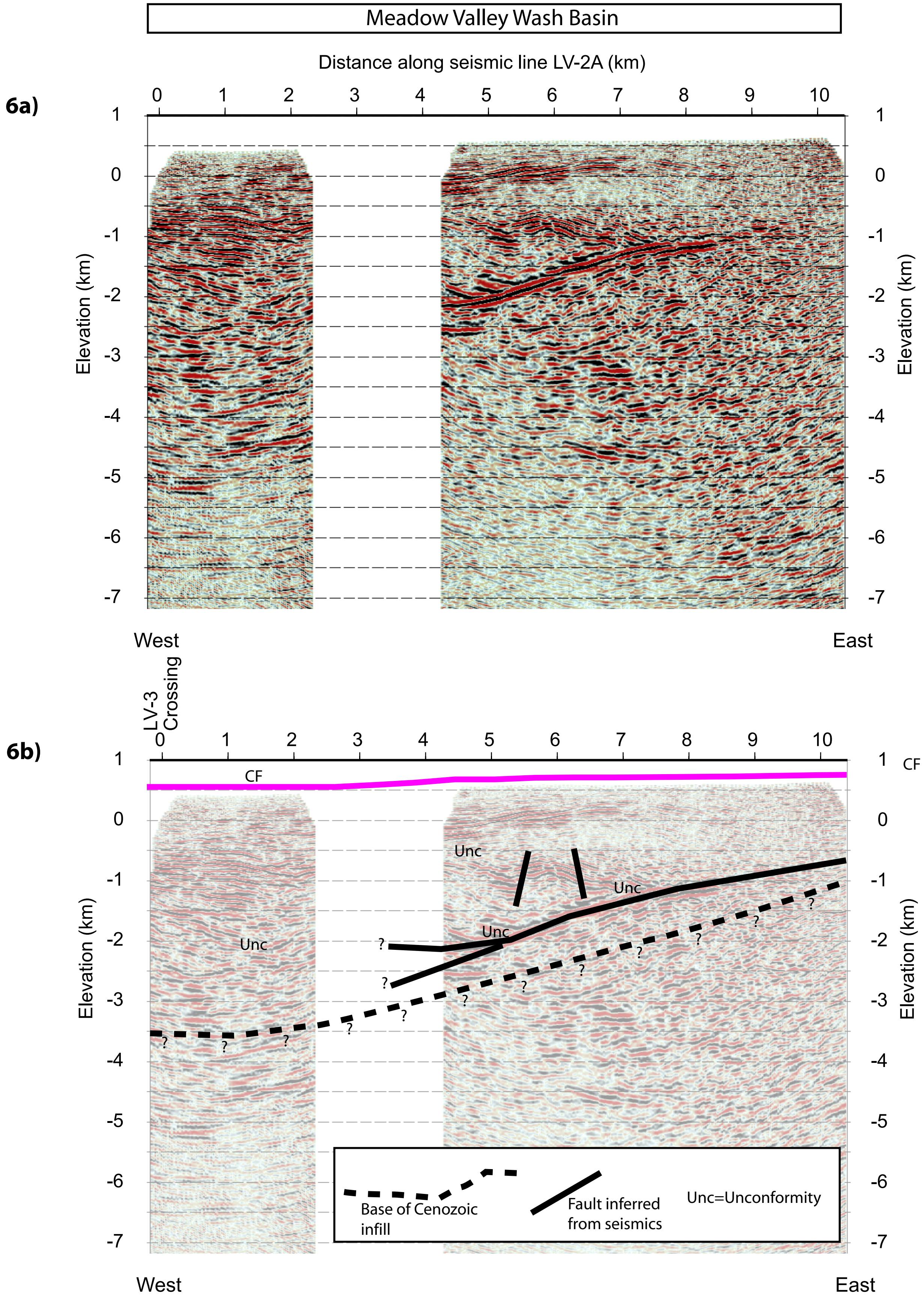

Figure 6. Migrated seismic reflection line LV-2A between southern Meadow Valley Wash and the southern Mormon Mountains, displayed with no vertical exaggeration. In the field notes from seismic acquisition, the portion of the line east of the data gap is named "LV-2A" and the portion to the west is named "LV-2A W-extension". During the seismic processing, all of the shots east and west of the gap were considered as one line, and in this report, the entire line is named LV-2A. (6a) Uninterpreted section. (6b) Interpreted section, with magenta line indicating land surface. Along-line distances in kilometers are east of LV-3 crossing. The base of the Cenozoic infill (dashed line) is speculative and is chosen to match its interpreted depth (~3.5 km below sea level) where LV-2A crosses LV-3.

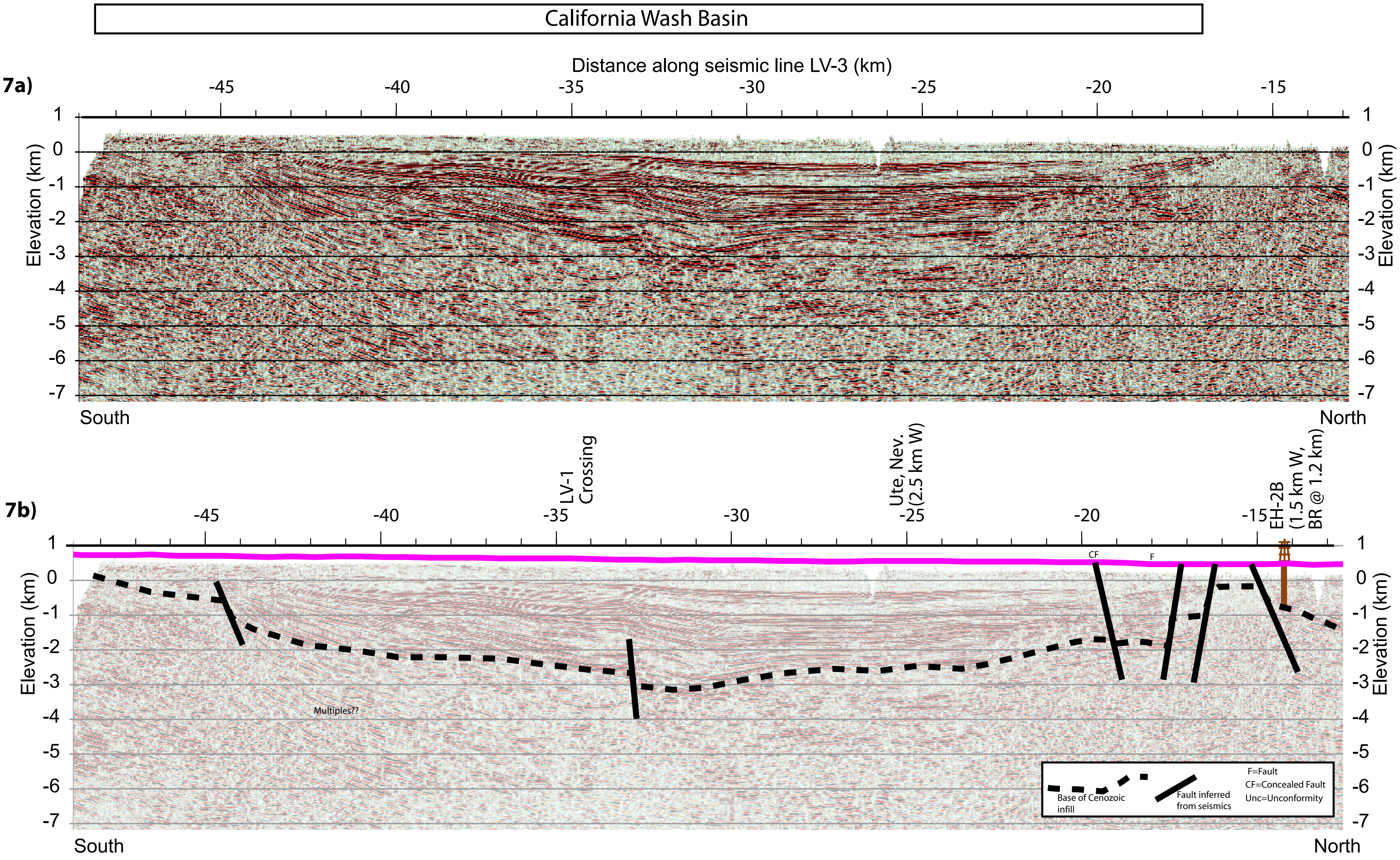

Figure 7. Migrated seismic reflection line LV-3 along California Wash, displayed with no vertical exaggeration. (7a) Uninterpreted section. (7b) Interpreted section, with magenta line indicating land surface. Along-line distances in kilometers are north of LV-2A crossing. BR, basement.

Table A1. Principal facts for gravity stations collected in April 2002 (MV and MW station names) and December 2002 (TD station names) in southern Nevada.

[Datums: latitude and longitude, NAD27; elevations, NGVD29. FAA, free-air gravity anomaly; ITC, inner terrain correction calculated out to 2 km; TTC, total terrain correction; CBA, complete Bouguer gravity anomaly, ISO, isostatic gravity anomaly]

Station	Latitude north (deg min)	Longitude west (deg min)	Elevation (m)	Observed gravity (mGal)	FAA (mGal)	ITC (mGal)	TTC (mGal)	CBA (mGal)	ISO (mGal)
MV001	36 37.95	-114 40.72	539.6	979653.20	-53.21	0.09	0.18	-114.09	-2.23
MV002	36 37.50	-114 41.58	551.0	979649.88	-52.35	0.10	0.21	-114.49	-2.53
MV003	36 37.02	-114 42.49	565.0	979644.33	-52.89	0.11	0.26	-116.57	-4.47
MV004	36 36.55	-114 43.39	573.9	979639.37	-54.43	0.11	0.32	-119.05	-6.74
MV005	36 36.10	-114 44.26	600.1	979632.65	-52.40	0.22	0.43	-119.87	-7.36
MV006	36 36.60	-114 45.10	609.2	979635.63	-47.35	0.20	0.53	-115.74	-2.45
MV007	36 41.05	-114 38.86	542.5	979653.75	-56.24	0.02	0.04	-117.58	-4.41
MV008	36 39.78	-114 38.41	494.1	979665.63	-57.45	0.05	0.14	-113.22	-1.07
MV009	36 38.74	-114 38.06	511.1	979659.87	-56.45	0.11	0.15	-114.15	-2.76
MV010	36 38.43	-114 39.05	521.0	979655.67	-57.16	0.06	0.11	-116.01	-4.54
MV011	36 37.58	-114 39.50	528.2	979654.20	-55.19	0.02	0.08	-114.88	-3.74
MV012	36 32.30	-114 43.94	600.1	979621.45	-58.14	0.02	0.10	-125.94	-15.60
MV013	36 32.82	-114 43.63	586.3	979623.18	-61.42	0.11	0.22	-127.54	-17.11
MV014	36 34.72	-114 42.44	576.4	979629.53	-60.85	0.07	0.15	-125.92	-15.11
MV015	36 34.20	-114 43.73	598.6	979624.30	-58.49	0.11	0.22	-126.00	-14.84
MV016	36 35.58	-114 47.59	781.2	979606.80	-21.64	1.59	2.02	-107.96	6.26
MV017	36 37.62	-114 51.70	964.7	979573.56	-1.21	2.18	3.69	-106.55	11.80
MV018	36 37.32	-114 50.86	887.9	979587.83	-10.21	0.60	2.03	-108.54	9.01
MV019	36 36.86	-114 49.87	827.2	979600.87	-15.21	0.09	1.05	-107.69	8.87
MV020	36 36.53	-114 49.06	776.6	979612.21	-19.01	0.06	0.74	-106.09	9.71
MV021	36 36.11	-114 48.15	720.8	979617.11	-30.73	0.18	0.70	-111.55	3.39
MV022	36 35.16	-114 47.24	693.7	979624.10	-30.72	0.05	0.39	-108.79	5.00
MV023	36 35.16	-114 46.10	675.1	979621.20	-39.35	0.02	0.26	-115.46	-2.39
MV024	36 35.63	-114 45.22	640.8	979623.99	-47.82	0.15	0.36	-119.96	-7.19
MV025	36 34.45	-114 45.88	649.4	979621.16	-46.31	0.13	0.35	-119.42	-6.90
MV026	36 34.51	-114 47.32	704.1	979620.98	-29.70	0.17	0.47	-108.87	4.57
MV027	36 34.53	-114 47.87	808.3	979599.16	-19.39	1.53	2.06	-108.74	5.06
MV028	36 33.56	-114 47.92	866.2	979583.01	-16.28	4.44	5.36	-108.85	4.44
MV029	36 33.93	-114 45.23	628.7	979621.06	-52.03	0.13	0.29	-122.87	-11.00
MV030	36 33.34	-114 46.01	638.4	979619.15	-50.12	0.09	0.29	-122.04	-10.01
MV031	36 32.69	-114 46.80	641.3	979620.62	-46.82	0.14	0.39	-118.98	-6.82
MV032	36 32.08	-114 47.54	647.9	979621.39	-43.13	0.17	0.43	-115.99	-3.73
MV033	36 31.45	-114 48.29	676.5	979619.39	-35.38	0.13	0.37	-111.54	0.84
MV034	36 30.65	-114 49.24	656.5	979622.38	-37.41	0.01	0.32	-111.36	1.18
MV035	36 31.68	-114 49.23	684.9	979618.08	-34.45	0.03	0.37	-111.55	1.58
MV036	36 35.11	-114 43.70	602.3	979626.72	-56.24	0.12	0.25	-124.13	-12.46
MV037	36 35.73	-114 42.92	584.1	979634.77	-54.70	0.02	0.13	-120.65	-9.05
MV038	36 36.30	-114 42.18	549.6	979643.19	-57.75	0.12	0.28	-119.66	-8.12
MV039	36 36.98	-114 41.33	550.0	979646.92	-54.87	0.08	0.17	-116.94	-5.42
MV040	36 37.56	-114 40.57	533.8	979652.39	-55.24	0.09	0.18	-115.47	-3.90
MV041	36 38.14	-114 39.80	525.0	979654.70	-56.49	0.08	0.15	-115.74	-4.13
MV042	36 38.67	-114 40.18	495.8	979663.83	-57.12	0.28	0.48	-112.76	-0.67
MV043	36 39.34	-114 39.80	485.9	979665.35	-59.61	0.17	0.39	-114.22	-1.87
MV044	36 39.15	-114 39.08	476.0	979665.07	-62.67	0.47	0.69	-115.86	-3.90
MV045	36 32.25	-114 42.01	560.0	979628.72	-63.15	0.12	0.23	-126.28	-16.95
MV046	36 31.41	-114 42.91	574.9	979624.31	-61.76	0.13	0.23	-126.58	-17.23
MV047	36 30.73	-114 43.69	587.8	979620.68	-60.42	0.15	0.24	-126.69	-17.29
MV048	36 30.20	-114 44.60	598.0	979619.09	-58.10	0.11	0.22	-125.54	-15.95
MV049	36 32.63	-114 40.76	569.9	979630.56	-58.83	0.10	0.17	-123.13	-14.08

MV050	36 32.78	-114 39.76	591.3	979628.83	-54.17	0.13	0.18	-120.89	-12.19
MV051	36 32.56	-114 38.60	623.5	979630.39	-42.35	0.19	0.28	-112.61	-4.44
MV052	36 32.65	-114 37.57	661.2	979626.14	-35.09	0.50	0.55	-109.34	-1.40
MV053	36 32.17	-114 34.76	759.9	979606.63	-23.45	0.82	0.99	-108.40	-1.35
MV054	36 32.49	-114 35.80	720.7	979614.51	-28.15	0.33	0.39	-109.26	-1.90
MV055	36 32.83	-114 36.50	691.6	979625.04	-27.09	0.50	0.57	-104.74	2.98
MV056	36 33.56	-114 38.92	599.1	979632.42	-49.30	0.18	0.23	-116.85	-8.06
MV057	36 40.35	-114 36.19	514.5	979664.39	-53.22	0.04	0.03	-111.41	0.54
MV058	36 39.88	-114 35.69	496.2	979667.34	-55.22	0.06	0.08	-111.30	0.22
MV059	36 40.84	-114 36.52	506.1	979662.23	-58.66	0.08	0.10	-115.84	-3.46
MV060	36 42.22	-114 35.57	465.9	979668.35	-66.93	0.10	0.36	-119.31	-6.09
MV061	36 41.24	-114 35.54	472.5	979669.17	-62.68	0.11	0.25	-115.91	-3.44
MV062	36 40.61	-114 35.09	460.1	979676.11	-58.66	0.09	0.26	-110.48	1.43
MV063	36 42.19	-114 36.74	495.0	979661.89	-64.39	0.08	0.20	-120.21	-6.74
MV064	36 41.88	-114 35.23	467.9	979669.02	-65.16	0.06	0.29	-117.83	-4.91
MV065	36 44.87	-114 36.52	497.8	979664.47	-64.82	0.04	0.43	-120.72	-5.08
MV066	36 44.12	-114 36.06	484.8	979665.28	-66.92	0.11	0.50	-121.30	-6.44
MV067	36 43.76	-114 35.79	483.7	979665.19	-66.84	0.12	0.48	-121.10	-6.58
MV068	36 43.38	-114 35.46	483.6	979664.73	-66.79	0.15	0.47	-121.05	-6.90
MV069	36 42.89	-114 35.55	473.8	979666.35	-67.48	0.09	0.39	-120.71	-6.96
MV070	36 42.26	-114 34.30	501.7	979659.90	-64.41	0.13	0.29	-120.90	-7.81
MV071	36 42.42	-114 33.38	575.3	979645.48	-56.36	0.24	0.27	-121.18	-8.10
MV072	36 43.04	-114 33.47	568.8	979646.73	-58.00	0.26	0.33	-122.03	-8.44
MV073	36 41.37	-114 34.46	467.9	979674.01	-59.43	0.07	0.28	-112.12	0.28
MV074	36 40.69	-114 34.47	461.0	979679.20	-55.39	0.07	0.25	-107.32	4.58
MV075	36 40.85	-114 33.44	486.2	979675.68	-51.39	0.13	0.24	-106.17	5.68
MV076	36 41.08	-114 32.37	543.2	979660.77	-49.04	0.15	0.15	-110.36	1.57
MV077	36 41.56	-114 31.57	521.5	979665.56	-51.62	0.39	0.52	-110.12	2.19
MV078	36 42.45	-114 30.14	644.3	979638.17	-42.41	0.31	0.34	-114.97	-2.00
MV079	36 42.06	-114 30.73	634.7	979641.80	-41.19	0.26	0.28	-112.71	-0.05
MV080	36 41.11	-114 31.15	711.4	979623.83	-34.12	4.11	4.54	-110.04	1.89
MV081	36 41.63	-114 30.21	630.1	979638.82	-44.96	0.06	0.09	-116.16	-3.87
MV082	36 38.93	-114 30.66	513.1	979656.85	-59.14	0.24	0.19	-117.02	-6.68
MV083	36 39.42	-114 31.37	575.9	979649.67	-47.64	0.47	0.43	-112.37	-1.67
MV084	36 38.70	-114 32.99	445.5	979679.44	-57.08	0.40	0.68	-106.82	3.47
MV085	36 39.52	-114 32.65	479.7	979675.70	-51.43	0.06	0.14	-105.59	5.25
MV086	36 38.39	-114 31.37	447.5	979673.16	-62.29	0.71	0.88	-112.07	-2.06
MV087	36 38.95	-114 35.85	513.1	979671.58	-44.43	0.12	0.14	-102.36	8.57
MV088	36 36.27	-114 39.45	541.1	979648.43	-55.08	0.04	0.09	-116.22	-5.84
MV089	36 33.37	-114 42.42	564.1	979629.32	-62.91	0.14	0.23	-126.51	-16.41
MV090	36 34.28	-114 42.70	586.6	979628.00	-58.60	0.01	0.08	-124.90	-14.22
MV091	36 33.50	-114 43.18	586.8	979626.54	-58.87	0.01	0.09	-125.17	-14.63
MV092	36 30.33	-114 42.65	601.1	979619.61	-56.82	0.00	0.05	-124.79	-16.07
MV093	36 30.36	-114 41.39	608.1	979620.58	-53.73	0.01	0.05	-122.49	-14.30
MV094	36 31.53	-114 40.49	594.1	979627.18	-53.14	0.01	0.06	-120.29	-11.92
MV095	36 32.23	-114 39.95	586.6	979629.53	-54.10	0.13	0.20	-120.27	-11.72
MW001	36 41.07	-114 40.95	505.6	979667.20	-54.19	0.15	0.42	-110.98	3.02
MW002	36 41.10	-114 39.83	498.7	979665.19	-58.37	0.08	0.26	-114.55	-0.97
MW003	36 41.49	-114 39.04	564.9	979653.16	-50.52	0.15	0.16	-114.29	-0.76
MW004	36 42.66	-114 41.82	522.5	979668.91	-49.55	0.11	0.45	-108.23	7.26
MW005	36 42.71	-114 42.87	534.4	979669.91	-44.97	0.25	0.72	-104.71	11.29
MW006	36 43.15	-114 43.67	578.6	979662.36	-39.50	0.24	0.63	-104.34	12.33
MW007	36 43.92	-114 46.82	582.4	979658.63	-43.19	3.48	4.33	-104.75	14.19
MW008	36 43.68	-114 46.08	572.0	979661.53	-43.14	2.15	2.97	-104.89	13.44
MW009	36 43.77	-114 45.31	565.1	979664.90	-42.04	1.18	1.87	-104.10	13.86
MW010	36 43.99	-114 44.65	560.8	979666.82	-41.75	0.36	0.99	-104.22	13.55
MW011	36 42.39	-114 42.96	585.0	979660.19	-38.60	0.24	0.52	-104.27	11.52
MW012	36 41.45	-114 42.53	569.5	979662.29	-39.92	0.22	0.49	-103.88	11.06

MW013	36 42.02	-114 42.67	574.5	979661.15	-40.34	0.15	0.42	-104.92	10.49
MW014	36 42.33	-114 43.54	594.7	979659.09	-36.64	0.28	0.61	-103.31	12.72
MW015	36 42.14	-114 44.60	641.0	979650.02	-31.13	0.37	0.72	-102.93	13.48
MW016	36 42.15	-114 45.67	677.3	979641.45	-28.52	0.34	0.73	-104.40	12.64
MW017	36 42.32	-114 46.69	715.2	979633.42	-25.12	0.53	0.95	-105.05	12.70
MW018	36 42.52	-114 47.53	791.2	979618.70	-16.68	0.51	0.98	-105.16	13.18
MW019	36 42.85	-114 47.69	919.2	979588.24	-8.13	4.60	5.79	-106.23	12.40
MW020	36 41.74	-114 46.49	713.7	979633.57	-24.58	0.65	1.09	-104.21	13.06
MW021	36 41.07	-114 46.88	751.8	979624.08	-21.35	0.53	1.00	-105.37	11.70
MW022	36 41.78	-114 40.87	506.6	979666.64	-55.45	0.11	0.38	-112.41	2.05
MW023	36 41.56	-114 40.85	505.8	979666.62	-55.42	0.12	0.39	-112.27	2.04
MW024	36 41.72	-114 40.07	563.8	979651.61	-52.74	0.24	0.28	-116.27	-2.16
MW025	36 42.38	-114 40.14	520.1	979662.54	-56.27	0.11	0.27	-114.85	-0.21
MW026	36 44.58	-114 44.42	562.5	979665.95	-42.94	0.21	0.81	-105.78	12.33
MW027	36 44.80	-114 44.15	602.4	979658.46	-38.45	0.17	0.54	-106.07	12.07
MW028	36 44.31	-114 43.51	555.8	979666.47	-44.11	0.13	0.59	-106.41	11.07
MW029	36 44.98	-114 43.08	576.3	979662.93	-42.28	0.04	0.39	-107.10	10.70
MW030	36 46.04	-114 43.35	618.0	979656.80	-37.08	0.17	0.54	-106.46	12.27
MW031	36 46.38	-114 42.74	642.5	979647.98	-38.83	0.09	0.36	-111.15	7.60
MW032	36 47.62	-114 43.20	697.3	979641.22	-30.48	0.76	1.06	-108.29	11.72
MW033	36 41.05	-114 38.85	542.5	979653.76	-56.23	0.02	0.04	-117.57	-4.40
MW034	36 40.18	-114 39.11	493.0	979664.75	-59.25	0.10	0.24	-114.80	-2.14
MW035	36 56.21	-114 39.20	626.5	979654.68	-51.28	0.29	1.50	-120.66	6.83
MW036	36 56.47	-114 38.14	696.7	979643.94	-40.74	0.57	1.51	-118.04	9.64
MW037	36 58.99	-114 37.74	644.1	979663.74	-40.83	1.77	3.60	-110.09	20.39
MW038	36 59.79	-114 37.27	653.4	979662.10	-40.77	2.05	4.02	-110.65	20.67
MW039	37 00.46	-114 36.86	676.0	979659.25	-37.60	1.49	3.40	-110.67	21.38
MW040	37 01.34	-114 35.86	690.5	979655.53	-38.14	3.27	5.40	-110.84	22.14
MW041	37 02.78	-114 34.50	725.2	979651.42	-33.61	0.95	2.93	-112.70	21.94
MW042	37 03.40	-114 33.67	735.3	979648.98	-33.85	1.00	2.95	-114.06	21.28
MW043	37 04.21	-114 33.68	761.3	979638.60	-37.38	2.00	3.53	-119.94	16.33
MW044	37 04.96	-114 33.58	800.9	979626.78	-38.06	1.23	2.40	-126.22	10.90
MW045	37 05.65	-114 32.98	846.0	979616.02	-35.90	0.38	1.20	-130.34	7.59
MW046	37 06.39	-114 32.40	884.3	979603.00	-38.17	0.35	0.97	-137.17	1.64
MW047	37 07.22	-114 32.12	917.4	979590.47	-41.71	0.29	0.79	-144.61	-4.83
MW048	37 07.89	-114 31.48	945.9	979579.37	-45.00	0.39	0.82	-151.08	-10.46
MW049	37 08.73	-114 31.34	976.9	979572.13	-43.87	0.14	0.55	-153.73	-12.11
MW050	37 09.42	-114 32.12	1020.5	979567.91	-35.65	0.06	0.46	-150.51	-8.06
MW051	37 08.11	-114 30.28	917.9	979582.68	-50.63	0.61	1.12	-153.26	-12.38
MW052	37 07.47	-114 29.45	805.5	979610.23	-56.83	0.37	1.47	-146.44	-6.26
MW053	37 08.57	-114 28.35	805.7	979602.65	-65.93	0.26	1.46	-155.58	-13.99
MW054	36 39.39	-114 40.86	505.5	979665.67	-53.32	0.15	0.38	-110.15	2.67
MW055	36 39.01	-114 40.28	500.6	979664.49	-55.47	0.11	0.30	-111.82	0.52
MW056	36 38.46	-114 41.07	525.6	979661.69	-49.77	0.17	0.33	-108.92	3.42
MW057	36 37.94	-114 41.95	570.0	979650.81	-46.19	0.03	0.13	-110.56	1.81
MW058	36 37.94	-114 43.10	590.2	979647.65	-43.13	0.02	0.19	-109.71	3.26
MW059	36 38.12	-114 44.11	608.9	979644.60	-40.67	0.02	0.28	-109.27	4.36
MW060	36 38.15	-114 45.15	640.3	979637.38	-38.24	0.04	0.41	-110.26	3.92
MW061	36 37.37	-114 44.28	612.3	979637.97	-45.16	0.04	0.28	-114.15	-0.92
MW062	36 36.59	-114 44.20	595.2	979637.69	-49.60	0.06	0.30	-116.64	-3.91
MW064	36 36.08	-114 49.52	776.1	979610.63	-20.10	0.05	0.83	-107.03	8.85
MW065	36 35.25	-114 49.93	763.0	979609.47	-24.11	0.05	0.92	-109.47	6.25
MW066	36 34.47	-114 50.30	784.8	979604.07	-21.66	0.06	0.88	-109.52	5.96
MW067	36 33.63	-114 50.73	783.2	979604.20	-20.80	0.22	0.98	-108.39	6.94
MW068	36 33.34	-114 51.48	801.0	979601.17	-17.93	1.24	2.07	-106.43	9.26
MW069	36 32.40	-114 51.12	712.4	979618.93	-26.14	0.31	1.03	-105.69	9.19
MW070	36 31.59	-114 51.44	665.1	979621.96	-36.53	0.41	1.18	-110.59	4.04
MW071	36 30.90	-114 52.08	632.8	979622.73	-44.74	0.03	0.96	-115.37	-0.69

MW072	36 30.28	-114 52.80	618.9	979623.25	-47.61	0.03	1.15	-116.48	-1.64
MW073	36 29.66	-114 53.48	637.2	979620.51	-43.81	0.10	1.27	-114.62	0.27
MW074	36 28.88	-114 54.07	638.9	979618.93	-43.74	0.14	1.38	-114.65	0.15
MW075	36 28.44	-114 55.01	661.2	979614.13	-41.05	1.19	2.60	-113.24	1.91
MW076	36 27.68	-114 54.59	618.3	979619.85	-47.46	0.17	1.47	-115.94	-1.61
MW077	36 26.88	-114 54.85	640.0	979613.63	-45.82	0.06	1.22	-117.00	-3.09
MW078	36 26.04	-114 55.14	681.6	979605.77	-39.64	0.09	1.03	-115.71	-2.23
MW079	36 26.22	-114 57.48	819.9	979576.37	-26.64	0.11	1.38	-117.96	-2.80
MW080	36 30.65	-114 56.71	817.3	979584.09	-26.12	0.60	2.18	-116.34	1.69
MW081	36 32.42	-114 56.10	805.4	979583.59	-32.81	0.01	1.56	-122.32	-3.52
MW082	36 34.24	-114 55.46	812.2	979591.66	-25.29	0.05	1.58	-115.55	3.89
MW083	36 36.19	-114 55.12	848.3	979586.62	-22.00	0.38	2.02	-115.88	4.51
MW084	36 37.95	-114 55.12	833.8	979593.62	-22.01	0.39	2.44	-113.83	7.60
MW085	36 40.62	-114 55.46	755.0	979610.44	-33.36	0.03	2.34	-116.40	6.85
MW086	36 30.36	-114 40.33	618.1	979622.85	-48.37	0.02	0.06	-118.24	-10.44
MW087	36 30.35	-114 39.27	654.3	979622.74	-37.31	0.05	0.10	-111.22	-3.81
MW088	36 30.17	-114 38.23	697.6	979618.42	-28.01	0.17	0.26	-106.66	0.34
MW089	36 30.59	-114 37.30	750.3	979608.39	-22.39	0.53	0.60	-106.64	0.28
MW090	36 31.34	-114 36.80	758.0	979609.19	-20.29	0.24	0.35	-105.66	1.41
MW091	36 32.07	-114 36.28	728.0	979615.76	-24.04	0.22	0.28	-106.09	1.22
MW092	36 32.94	-114 35.65	776.4	979604.72	-21.40	0.45	0.67	-108.52	-0.96
MW093	36 33.68	-114 35.16	738.0	979614.21	-24.82	0.94	1.07	-107.21	0.56
MW094	36 34.43	-114 34.65	672.1	979630.20	-30.24	0.42	0.49	-105.78	2.28
MW095	36 35.23	-114 34.25	610.3	979644.05	-36.61	0.47	0.59	-105.07	3.38
MW096	36 35.99	-114 33.82	568.5	979652.39	-42.27	0.76	0.84	-105.75	3.03
MW097	36 36.69	-114 33.20	531.6	979660.33	-46.72	0.62	0.74	-106.14	2.96
MW098	36 37.48	-114 32.78	498.4	979670.87	-47.55	0.58	0.69	-103.27	6.25
MW099	36 38.39	-114 32.63	452.5	979678.66	-55.23	0.45	0.69	-105.76	4.30
MW100	36 37.26	-114 36.04	567.2	979658.89	-37.99	0.10	0.15	-102.02	7.87
MW101	36 36.45	-114 35.53	677.1	979633.62	-28.17	0.62	0.71	-104.06	5.25
MW102	36 35.45	-114 35.88	808.9	979605.69	-14.01	1.71	2.45	-103.02	5.79
MW103	36 35.95	-114 35.41	739.7	979621.87	-19.90	0.51	0.84	-102.72	6.30
TD001	36 58.86	-114 19.70	992.2	979589.75	-7.23	0.06	0.93	-118.43	11.94
TD002	36 58.82	-114 19.57	986.2	979590.60	-8.18	0.06	0.90	-118.73	11.59
TD003	36 58.78	-114 19.45	979.4	979591.72	-9.12	0.06	0.88	-118.92	11.37
TD004	36 58.75	-114 19.31	974.3	979592.42	-9.95	0.06	0.85	-119.20	11.07
TD005	36 58.71	-114 19.19	968.9	979593.45	-10.51	0.07	0.85	-119.16	11.08
TD006	36 58.68	-114 19.06	962.8	979594.88	-10.93	0.09	0.85	-118.89	11.31
TD007	36 58.63	-114 18.94	956.6	979596.65	-11.00	0.13	0.88	-118.23	11.92
TD008	36 58.58	-114 18.82	951.2	979598.58	-10.65	0.20	0.94	-117.21	12.89
TD009	36 58.50	-114 18.69	942.8	979601.41	-10.30	0.29	1.04	-115.81	14.23
TD010	36 58.47	-114 18.57	930.6	979604.21	-11.23	0.46	1.24	-115.17	14.84
TD011	36 58.49	-114 18.43	935.9	979603.38	-10.44	0.39	1.12	-115.10	14.94
TD012	36 58.45	-114 18.31	925.5	979605.32	-11.66	0.45	1.19	-115.07	14.96
TD013	36 58.38	-114 18.20	908.6	979608.86	-13.23	0.80	1.59	-114.34	15.61
TD014	36 58.46	-114 18.03	901.0	979610.64	-13.89	0.61	1.39	-114.35	15.71
TD015	36 58.44	-114 17.90	893.9	979612.14	-14.58	0.67	1.46	-114.17	15.87
TD016	36 58.41	-114 17.73	888.3	979613.38	-15.02	0.61	1.38	-114.05	15.99
TD017	36 58.38	-114 17.59	884.9	979614.13	-15.28	0.56	1.32	-113.98	16.04
TD018	36 58.33	-114 17.47	879.9	979615.04	-15.83	0.63	1.39	-113.90	16.08
TD019	36 58.25	-114 17.37	874.2	979616.24	-16.26	0.68	1.46	-113.63	16.28
TD020	36 58.26	-114 17.21	867.6	979617.17	-17.38	0.58	1.35	-114.12	15.80
TD021	36 58.25	-114 17.07	862.8	979617.70	-18.34	0.49	1.24	-114.63	15.29
TD022	36 58.21	-114 16.94	858.0	979617.91	-19.53	0.45	1.19	-115.34	14.55
TD023	36 58.18	-114 16.81	853.5	979618.22	-20.56	0.40	1.12	-115.93	13.95
TD024	36 58.16	-114 16.68	850.1	979618.66	-21.17	0.39	1.09	-116.18	13.70
TD025	36 58.11	-114 16.55	846.0	979619.35	-21.66	0.40	1.07	-116.23	13.61
TD026	36 58.09	-114 16.42	843.0	979619.84	-22.08	0.35	0.99	-116.39	13.44

TD027	36 58.05	-114 16.30	839.2	979620.51	-22.51	0.36	0.98	-116.41	13.40
TD028	36 58.00	-114 16.17	835.6	979620.99	-23.06	0.41	1.01	-116.52	13.28
TD029	36 57.90	-114 16.09	830.7	979622.02	-23.41	0.34	0.95	-116.38	13.32
TD030	36 57.86	-114 15.94	825.3	979622.83	-24.19	0.43	1.02	-116.48	13.19
TD031	36 57.81	-114 15.83	822.1	979623.32	-24.62	0.41	0.98	-116.60	13.04
TD032	36 57.77	-114 15.72	817.3	979624.09	-25.29	0.50	1.06	-116.64	12.99
TD033	36 57.70	-114 15.61	812.9	979624.90	-25.73	0.45	1.00	-116.64	12.94
TD034	36 57.62	-114 15.50	809.4	979625.44	-26.15	0.39	0.93	-116.74	12.77
TD035	36 57.54	-114 15.40	805.2	979626.16	-26.61	0.49	1.02	-116.63	12.78
TD036	36 57.53	-114 15.26	801.2	979626.67	-27.32	0.48	0.99	-116.92	12.51
TD037	36 57.55	-114 15.09	796.7	979627.40	-28.01	0.50	0.98	-117.11	12.35
TD038	36 57.56	-114 14.92	792.0	979627.97	-28.90	0.57	1.02	-117.43	12.06
TD039	36 57.56	-114 14.71	786.0	979629.02	-29.70	0.67	1.10	-117.48	12.06
TD040	36 57.49	-114 14.53	780.4	979629.92	-30.41	0.68	1.10	-117.56	11.96
TD041	36 57.34	-114 14.33	773.4	979630.97	-31.31	0.59	0.99	-117.77	11.61
TD042	36 57.30	-114 14.13	765.2	979631.68	-33.09	0.69	1.09	-118.53	10.86
TD043	36 58.40	-114 19.68	989.6	979589.63	-7.50	0.07	0.94	-118.39	11.42
TD044	36 58.42	-114 19.82	995.5	979588.53	-6.81	0.07	0.98	-118.33	11.50
TD045	36 58.44	-114 19.95	1001.9	979587.48	-5.90	0.06	1.00	-118.12	11.74
TD046	36 58.46	-114 20.08	1008.4	979586.41	-5.01	0.07	1.03	-117.93	11.94
TD047	36 58.48	-114 20.21	1013.3	979585.74	-4.20	0.07	1.07	-117.63	12.25
TD048	36 58.51	-114 20.35	1019.7	979584.74	-3.25	0.08	1.12	-117.36	12.54
TD049	36 58.51	-114 20.48	1025.0	979584.01	-2.37	0.07	1.15	-117.03	12.87
TD050	36 58.53	-114 20.62	1031.6	979582.96	-1.41	0.08	1.21	-116.76	13.13
TD051	36 58.55	-114 20.75	1037.4	979582.09	-0.50	0.09	1.26	-116.46	13.45
TD052	36 58.57	-114 20.88	1043.8	979581.12	0.48	0.13	1.34	-116.12	13.79
TD053	36 58.60	-114 21.01	1050.9	979580.12	1.60	0.15	1.40	-115.73	14.21
TD054	36 58.63	-114 21.14	1057.6	979579.21	2.73	0.20	1.49	-115.27	14.68
TD055	36 58.65	-114 21.27	1063.6	979578.10	3.44	0.24	1.57	-115.16	14.81
TD056	36 58.68	-114 21.40	1071.1	979576.34	3.94	0.26	1.62	-115.45	14.55
TD057	36 58.70	-114 21.74	1092.1	979572.36	6.41	0.39	1.81	-115.16	14.83
TD058	36 58.67	-114 22.08	1112.3	979568.78	9.10	0.67	2.17	-114.37	15.59
TD059	36 58.53	-114 22.43	1128.2	979565.92	11.37	1.05	2.69	-113.38	16.37
TD060	36 58.52	-114 22.74	1156.0	979559.87	13.91	0.50	2.23	-114.43	15.30
TD061	36 58.50	-114 23.07	1175.1	979556.68	16.62	0.38	2.27	-113.82	15.87
TD062	36 58.27	-114 23.36	1205.3	979551.17	20.77	0.46	2.50	-112.84	16.57
TD063	36 58.08	-114 23.65	1238.7	979545.04	25.21	0.44	2.64	-112.02	17.13
TD064	36 57.96	-114 23.97	1272.8	979538.85	29.72	0.52	2.93	-111.07	17.91
TD065	37 01.57	-114 17.95	875.9	979614.89	-21.89	0.31	1.00	-119.91	13.62
TD066	37 01.49	-114 17.86	868.2	979617.09	-21.96	0.66	1.38	-118.72	14.75
TD067	37 01.45	-114 17.73	865.4	979617.03	-22.83	1.06	1.77	-118.89	14.54
TD068	37 01.40	-114 17.61	863.0	979617.04	-23.47	1.15	1.85	-119.19	14.21
TD069	37 01.34	-114 17.49	860.8	979617.53	-23.59	0.76	1.45	-119.46	13.86
TD070	37 01.29	-114 17.37	859.0	979617.47	-24.12	0.50	1.17	-120.06	13.21
TD071	37 01.29	-114 17.22	857.1	979616.06	-26.13	0.35	1.01	-122.02	11.28
TD072	37 01.27	-114 17.09	854.9	979616.39	-26.45	0.32	0.97	-122.13	11.13
TD073	37 01.22	-114 16.96	853.4	979617.13	-26.10	0.30	0.93	-121.65	11.57
TD074	37 01.20	-114 16.83	850.9	979618.06	-25.92	0.34	0.96	-121.15	12.05
TD075	37 01.65	-114 18.04	879.0	979613.54	-22.43	0.22	0.91	-120.88	12.73
TD076	37 01.70	-114 18.17	887.5	979611.18	-22.22	0.14	0.81	-121.74	11.91
TD077	37 01.72	-114 18.31	893.9	979609.88	-21.57	0.09	0.75	-121.87	11.80
TD078	37 01.73	-114 18.46	894.5	979609.75	-21.55	0.10	0.80	-121.86	11.82
TD079	37 01.77	-114 18.58	896.9	979609.17	-21.42	0.08	0.80	-122.01	11.70
TD080	37 01.77	-114 18.73	904.0	979607.77	-20.63	0.05	0.78	-122.04	11.67
TD081	37 01.78	-114 18.86	905.4	979607.54	-20.45	0.07	0.83	-121.96	11.77
TD082	37 01.82	-114 18.99	915.3	979605.39	-19.60	0.04	0.79	-122.27	11.49
TD083	37 01.87	-114 19.11	919.2	979604.37	-19.50	0.04	0.81	-122.59	11.23
TD084	37 01.92	-114 19.24	922.6	979603.33	-19.55	0.05	0.85	-122.99	10.89

TD085	37 01.96	-114 19.36	928.8	979601.98	-19.06	0.06	0.87	-123.17	10.75
TD086	37 02.00	-114 19.48	936.4	979600.63	-18.13	0.08	0.89	-123.07	10.89
TD087	37 02.04	-114 19.60	946.0	979598.88	-16.98	0.11	0.93	-122.96	11.02
TD088	37 02.09	-114 19.74	949.0	979598.14	-16.86	0.11	0.98	-123.14	10.88
TD089	37 02.14	-114 19.86	957.0	979596.28	-16.33	0.14	1.02	-123.46	10.60
TD090	37 02.17	-114 19.98	964.1	979594.41	-16.05	0.17	1.09	-123.92	10.17
TD091	37 02.23	-114 20.10	970.2	979592.76	-15.89	0.21	1.15	-124.39	9.76
TD092	37 02.27	-114 20.22	979.5	979590.71	-15.15	0.26	1.22	-124.62	9.57
TD093	37 02.28	-114 20.35	986.1	979589.89	-13.95	0.41	1.41	-123.97	10.22
TD094	37 01.12	-114 16.72	848.8	979618.43	-26.06	0.25	0.87	-121.15	11.99
TD095	37 01.05	-114 16.63	847.0	979618.96	-25.99	0.21	0.83	-120.92	12.15
TD096	37 00.93	-114 16.60	844.8	979619.21	-26.25	0.23	0.85	-120.91	12.02
TD097	37 00.88	-114 16.45	841.5	979619.98	-26.42	0.20	0.82	-120.74	12.15
TD098	37 00.82	-114 16.35	840.4	979620.12	-26.54	0.16	0.76	-120.79	12.04
TD099	37 01.02	-114 16.16	872.5	979614.08	-22.96	0.08	0.51	-121.09	11.99
TD100	37 00.95	-114 16.05	863.5	979616.29	-23.42	0.09	0.53	-120.52	12.48
TD101	37 00.92	-114 15.85	873.8	979614.63	-21.86	0.06	0.43	-120.21	12.78
TD102	37 00.89	-114 15.65	872.5	979615.38	-21.48	0.05	0.40	-119.71	13.29
TD103	37 01.06	-114 15.42	876.9	979614.74	-20.99	0.05	0.38	-119.75	13.46
TD104	37 00.86	-114 15.24	875.4	979614.94	-20.98	0.04	0.35	-119.59	13.41
TD105	37 00.74	-114 15.12	872.3	979615.20	-21.51	0.05	0.35	-119.76	13.09
TD106	37 05.37	-114 19.38	946.3	979595.17	-25.40	0.01	0.35	-132.00	5.96
TD107	37 05.86	-114 17.17	981.8	979585.58	-24.78	0.01	0.24	-135.49	3.17
TD108	37 07.01	-114 16.32	1018.7	979574.17	-26.45	0.02	0.25	-141.31	-1.19
TD109	37 08.78	-114 15.12	1080.7	979561.21	-22.86	0.02	0.30	-144.66	-2.20
TD110	37 10.04	-114 14.44	1124.5	979551.99	-20.40	0.03	0.35	-147.08	-2.95
TD111	37 11.00	-114 13.01	1177.7	979539.19	-18.19	0.03	0.37	-150.82	-5.28
TD112	37 10.83	-114 08.42	1129.3	979561.20	-10.84	0.35	0.68	-137.73	8.33
TD113	37 11.40	-114 11.48	1179.0	979543.39	-14.16	0.06	0.40	-146.92	-0.68
TD114	37 10.52	-114 15.06	1139.6	979548.71	-19.70	0.03	0.39	-148.04	-3.35
TD115	37 10.04	-114 16.36	1110.3	979556.95	-19.81	0.03	0.42	-144.82	-0.87
TD116	37 09.61	-114 17.71	1094.5	979562.08	-18.93	0.04	0.45	-142.13	1.14
TD117	37 09.23	-114 19.04	1076.7	979563.16	-22.80	0.05	0.47	-143.97	-1.26
TD118	37 09.05	-114 19.79	1066.4	979563.11	-25.77	0.05	0.47	-145.78	-3.34
TD119	37 08.72	-114 22.14	1049.1	979569.82	-23.92	0.04	0.46	-141.99	-0.11
TD120	37 08.90	-114 22.53	1057.2	979568.63	-22.86	0.05	0.49	-141.82	0.26
TD121	37 08.83	-114 23.92	1035.2	979575.57	-22.60	0.16	0.60	-138.97	2.96
TD122	37 09.05	-114 25.10	1011.1	979575.84	-30.09	0.05	0.54	-143.80	-1.62
TD127	37 07.17	-114 18.14	1002.4	979581.35	-24.55	0.02	0.28	-137.54	2.63
TD128	37 07.95	-114 16.75	1040.7	979571.11	-24.09	0.02	0.28	-141.40	-0.10
TD129	37 10.01	-114 19.55	1126.1	979547.65	-24.20	0.08	0.62	-150.79	-7.15
TD130	37 10.55	-114 19.42	1163.1	979537.74	-23.49	0.09	0.71	-154.14	-9.82
TD131	37 11.89	-114 19.37	1253.2	979517.92	-17.46	0.44	1.27	-157.69	-11.67
TD132	37 12.17	-114 19.34	1272.8	979514.56	-15.17	0.39	1.27	-157.62	-11.22
TD133	37 12.44	-114 19.46	1293.3	979509.69	-14.11	0.46	1.40	-158.72	-12.00
TD134	37 12.69	-114 19.72	1316.3	979504.46	-12.61	0.66	1.65	-159.56	-12.58
TD135	37 12.90	-114 19.96	1338.6	979501.75	-8.75	0.50	1.53	-158.33	-11.11
TD136	37 13.14	-114 20.11	1358.1	979499.15	-5.69	0.75	1.81	-157.18	-9.67
TD137	37 13.18	-114 20.48	1382.2	979494.34	-3.11	0.68	1.77	-157.36	-9.84
TD138	37 13.27	-114 20.79	1402.6	979489.72	-1.57	0.60	1.74	-158.14	-10.56
TD139	37 13.52	-114 21.41	1390.5	979492.03	-3.36	0.67	1.82	-158.48	-10.60
TD140	37 13.80	-114 21.55	1385.5	979492.40	-4.95	0.51	1.69	-159.63	-11.39
TD141	37 13.64	-114 18.91	1429.2	979483.25	-0.39	0.39	1.66	-160.02	-11.79
TD142	37 13.91	-114 18.99	1463.4	979476.12	2.65	0.62	1.99	-160.49	-11.93
TD143	37 14.40	-114 18.82	1528.5	979460.76	6.63	1.22	2.81	-163.00	-13.84
TD144	37 08.92	-114 17.36	1062.8	979568.49	-21.30	0.04	0.37	-141.01	1.43
TD145	37 02.80	-114 22.90	1153.0	979561.05	7.94	1.17	2.30	-119.99	14.62
TD146	37 03.28	-114 22.60	1112.8	979567.71	1.52	0.33	1.31	-122.88	12.32

TD147	37 03.76	-114 22.33	1071.8	979575.18	-4.35	0.29	1.07	-124.37	11.40

Table A2. Physical property measurements of rock samples collected in April 2002 (MV and MW sample names) and December 2002 (TD sample names) in southern Nevada.

[Latitude and longitude use NAD27 datum]

Sample ID	Rock type	Latitude north (deg min)	Longitude west (deg min)	Grain density (g/cm^3)	Saturated bulk density (g/cm^3)	Dry bulk density (g/cm^3)	Susceptibility (10^{-3} SI)
MWR1	carbonate	36 43.93	-114 47.05	2.70	2.69	2.68	0.00
MWR2	clastic	37 00.46	-114 36.86	2.65	2.59	2.55	0.13
MWR3	felsic volcanic	37 04.96	-114 33.58	2.43	2.20	2.04	0.25
MWR4A	carbonate	36 33.34	-114 51.48	2.84	2.84	2.83	0.00
MWR4B	carbonate	36 33.34	-114 51.48	2.72	2.70	2.70	0.00
MWR5A	clastic	36 32.07	-114 36.28	2.66	2.60	2.55	0.13
MWR5B	clastic	36 32.07	-114 36.28	2.60	2.48	2.41	0.13
MV017	carbonate	36 37.62	-114 51.70	2.85	2.85	2.84	0.00
MV028A	carbonate	36 33.56	-114 47.92	2.70	2.69	2.68	0.00
MV028B	carbonate	36 33.56	-114 47.92	2.59	2.51	2.45	0.00
MV080	carbonate	36 41.11	-114 31.15	2.83	2.81	2.81	0.00
MV083	carbonate	36 39.42	-114 31.37	2.70	2.67	2.66	0.00
TD013	felsic intrusive	36 58.38	-114 18.20	2.64	2.59	2.56	2.51
TD014	metamorphic	36 58.46	-114 18.03	2.81	2.77	2.74	11.3
TD014	metamorphic	36 58.46	-114 18.03	2.81	2.79	2.77	12.4
TD014	metamorphic	36 58.46	-114 18.03	2.79	2.72	2.68	12.9
TD015	felsic intrusive	36 58.44	-114 17.90	2.65	2.59	2.56	2.39
TD015	felsic intrusive	36 58.44	-114 17.90	2.65	2.63	2.61	4.02
TD015	felsic intrusive	36 58.44	-114 17.90	2.63	2.57	2.54	0.00
TD015	felsic intrusive	36 58.44	-114 17.90	2.61	2.59	2.57	0.38
TD018	quartzite	36 58.33	-114 17.47	2.65	2.63	2.61	0.00
TD019	felsic intrusive	36 58.25	-114 17.37	2.68	2.64	2.62	4.40
TD020	quartzite	36 58.26	-114 17.21	2.66	2.64	2.63	0.00
TD066	carbonate	37 01.49	-114 17.86	2.84	2.82	2.82	0.00
TD066	carbonate	37 01.49	-114 17.86	2.82	2.80	2.80	0.00
TD066	carbonate	37 01.49	-114 17.86	2.68	2.65	2.64	0.00
TD087	carbonate	37 02.04	-114 19.60	2.61	2.49	2.41	0.00
TD087	carbonate	37 02.04	-114 19.60	2.67	2.64	2.61	0.00
TD105	felsic volcanic	37 00.74	-114 15.12	2.61	2.49	2.41	0.13
TD131	felsic volcanic	37 11.89	-114 19.37	2.25	2.06	1.90	0.13
TD131	felsic volcanic	37 11.89	-114 19.37	2.26	2.06	1.90	0.13
TD135	felsic volcanic	37 12.90	-114 19.96	2.22	1.98	1.78	0.00